THE DEVELOPMENT AND APPLICATION OF SENSITIVITY TOOLS FOR INVESTIGATING MICROPHYSICAL PROCESSES IN ATMOSPHERIC MODELS

A Thesis
Presented to
The Academic Faculty

by

Benjamin Andrew Sheyko

In Partial Fulfillment
of the Requirements for the Degree
Masters of Science in the
School of Chemical and Biomolecular Engineering

Georgia Institute of Technology
December 2014

COPYRIGHT 2014 BY BENJAMIN ANDREW SHEYKO

THE DEVELOPMENT AND APPLICATION OF SENSITIVITY TOOLS FOR INVESTIGATING MICROPHYSICAL PROCESSES IN ATMOSPHERIC MODELS

Approved by:

Dr. Athanasios Nenes, Advisor
School of Chemical and Biomolecular Engineering
Georgia Institute of Technology

Dr. Pradeep Agrawal
School of Chemical and Biomolecular Engineering
Georgia Institute of Technology

Dr. Nga Lee (Sally) Ng
School of Chemical and Biomolecular Engineering
Georgia Institute of Technology

Dr. Armistead Russell
School of Civil and Environmental Engineering
Georgia Institute of Technology

Date Approved: July 9, 2014

To my family, Erika, and Mia

ACKNOWLEDGEMENTS

I would also like to thank Shannon Capps for teaching me how to use automatic differentiation software, Ricardo Morales for teaching me about atmospheric modeling, and the rest of the Nenes group for their help. I would like to thank my family and friends for their support through this process as well. In addition I would like to thank my funding sources, NASA, The Department of Energy, and the Phillips 66 Company.

TABLE OF CONTENTS

LIST OF TABLES

Page

LIST OF FIGURES

Page

LIST OF SYMBOLS AND ABBREVIATIONS

$\overline{\Gamma}$	Effective growth parameter [4]
$\lvert\partial N_i/\partial x_j\rvert$	Absolute value of the annually averaged sensitivity of N_i to field x_j
$\partial N_i/\partial x_j$	Sensitivity of formed crystal number concentration to field x_j
$\partial N_i/\partial x_j\rvert_n$	Normalized sensitivity of formed crystal number concentration to field x_j
∂N_i	Differential perturbation in formed crystal number concentration
∂x_j	Differential perturbation in field x_j
ΔS_{char}	Parameter related to the characteristic freezing threshold of insoluble aerosol
$dN_{IN,i}/dlogD_i$	Insoluble aerosol size distribution for species i
α	Updraft influenced supersaturation generation parameter [4]
α_d	Water vapor deposition coefficient for ice
β	Water vapor deposition parameter [4]
λ	Parameter related to the cooling rate provided by expansion work
$\xi N_i,x_j$	Percent contribution to σN_i from field x_j
ρ_a	Density of air
ρ_i	Density of ice
σ_g	Geometric standard deviation of a given aerosol size distribution
$\sigma N_{i,j}$	Variability of formed ice crystal number concentration from field x_j
σN_i	Total variability of formed ice crystal number concentration
σx_j	Standard deviation of field x_j
$\sigma x_j\rvert_n$	Normalized standard deviation of field x_j
μ_g	Geometric mean diameter of a given aerosol size distribution

μ_i	Number of ice embryos per insoluble aerosol particle of species *i*
φ	Crystal diameter growth rate parameter [5]
a	Coefficient related to the power law dependence of f_c on *w* from Equation 4
ABN09	Adjoint model of BN09
b	Exponent related to the power law dependence of f_c on *w* from Equation 4
BN09	Barahona and Nenes cirrus formation parameterization family
CAM 5.1	CESM Community Atmosphere Model Version 5.1
CCN	Cloud condensation nuclei
CTM	Chemical Transport Model
D_{bc}	Geometric mean diameter of black carbon aerosol
$D_{dust,a}$	Geometric mean diameter of dust aerosol in the accumulation mode
$D_{dust,c}$	Geometric mean diameter of dust aerosol in the coarse mode
D_{org}	Geometric mean diameter of organic carbon aerosol
D_{sulf}	Geometric mean diameter of sulfate aerosol
D_i	Geometric mean diameter of an insoluble aerosol size distribution of species *i*
$D_{min,i}$	Minimum diameter of an insoluble aerosol allowed to freeze of species *i*
f_c	Fraction of supercooled droplets that freeze homogeneously
F_{IN}	The number of crystals that freeze heterogeneously at a given thermodynamic state
GLOMAP	GLObal Model of Aerosol Processes model
GMI	NASA Global Modeling Initiative
GOCART	Goddard Chemistry Aerosol Radiation and Transport
i	Index of summation in Equation 5
IN	Ice nuclei

j	Index of summation in Equation 8
$k(T)$	Ice germ nucleation rate coefficient parameter [6, 7]
N^*	Parameter related to the rate change in surface area of the crystal population
N_{bc}	Number concentration of black carbon aerosol
N_d	Cloud droplet number concentration
$N_{dust,a}$	Number concentration of dust aerosol in the accumulation mode
$N_{dust,c}$	Number concentration of dust aerosol in the coarse mode
N_i	Formed ice crystal number concentration
$\overline{N_i}$	Annually averaged formed ice crystal number concentration
$N_{i,het}$	Formed crystal number concentration from heterogeneous freezing
$N_{i,hom}$	Formed crystal number concentration from homogeneous freezing
N_{lim}	Limiting number of ice nuclei needed to inhibit homogeneous freezing
N_o	Number concentration of supercooled soluble aerosol droplets
N_{org}	Number concentration of organic carbon aerosol
N_{sulf}	Number concentration of sulfate aerosol
$N_{total\ dust}$	Number concentration of accumulation and coarse mode dust aerosol
P	Pressure
PCNR	Post convergence Newton-Raphson Method
PDA 2008	Heterogeneous freezing spectrum used in this work
S_{hom}	Supersaturation threshold for homogeneous freezing
S_i	Supersaturation with respect to ice
S_{max}	Maximum in-cloud supersaturation reached during cloud formation
S^*_{max}	Converged maximum supersaturation from the bisection method

$S_{max,NR}$	Maximum supersaturation computed from the Newton-Raphson step
T	Temperature
TLM	Tangent linear model
TKE	Turbulent kinetic energy
w	Updraft velocity
x_i	Independent input variable to BN09
x_j	Independent input variable to BN09 that varies over CAM 5.1 simulations
$\overline{x}_j$	Local annual average of field x_j

SUMMARY

We present the development of the adjoint of a physically based cirrus formation parameterization that computes the sensitivity of formed crystal number concentration to numerous model variables (e.g., updraft velocity, soluble aerosol geometric mean diameter and number concentration, insoluble aerosol geometric mean diameter and number concentration, and ice deposition coefficient). The adjoint is demonstrated in the CESM Community Atmosphere Model Version 5.1, where sensitivity information is computed and used to quantify which variables are most responsible for modeled variability in formed crystal number concentration. The sensitivity of formed crystal number concentration to updraft velocity is positive and largest over the tropics where regions of deep convection are collocated with large sulfate number concentrations. Sensitivity to sulfate number concentration is largest over the tropics where updraft cooling is sufficient and sulfate number concentration is low, pointing to a sulfate limited regime. Outside of the tropics, crystal production is dominated by heterogeneous freezing; unexpectedly, sensitivities to insoluble aerosol number concentration for accumulation and coarse mode dust, black carbon, and organic carbon are negative in sign here. This is a result of infrequent, anomalously high updraft velocity events causing shifts in the dominant modes of freezing which act to bias sensitivity information when annually averaged. Updraft velocity is responsible for ~95% of the variability in formed crystal number concentration in the high latitudes of the Northern Hemisphere. In the tropics, sulfate number concentration controls variability in formed crystal number concentration since crystal production here is sulfate limited. Insoluble aerosol species

play a secondary role in influencing the variability of crystal concentrations; coarse mode dust is the largest contributor to crystal number variability at nearly 60%, although the spatial extent of this influence is small and concentrated over highly localized dust events. When globally averaged, nearly 90% of the variability in crystal number concentration can be described by only updraft velocity, sulfate number, temperature, and coarse mode dust number concentration. Although these results depend on parameter assumptions, the robustness of the underlying physics of the cirrus formation parameterization used throughout this work suggests that this approach can be a powerful method for efficiently identifying the origin of microphysical dependencies within large scale atmospheric simulations.

CHAPTER 1

INTRODUCTION

Anthropogenic activity can influence the state of the climate system [2]. In the last century, increased combustion and power generation have resulted in unprecedented emissions of greenhouse and reactive gasses as well as particulate matter (aerosol). These species change the composition of the atmosphere which can alter the radiative properties of Earth, leading to planetary warming or cooling. When compared to preindustrial times, the mean surface temperature of Earth has increased by 0.5 °C; much of this is believed to be a result of anthropogenic influences. Small temperature shifts like this can have profound impacts on features of the climate system including sea level, atmospheric water content, and planetary albedo. Because of this, the ability to accurately predict how the climate will respond to outside forcings over climatologically relevant temporal and spatial scales has become of increased interest. Unfortunately, achieving this remains challenging due to the vast, highly-coupled nature of the climate system. Additionally, key climate processes occur on spatial and temporal scales spanning orders of magnitude, making simulating such systems challenging. Of the climate features that play into the radiative energy balance of Earth and that are influenced by anthropogenic factors, the formation and persistence of clouds remains one of the most uncertain. Although this is a result of uncertainties in anthropogenic emissions and limitations in computational capabilities, much of this uncertainty stems from the physical description of cloud processes in atmospheric models. This thesis work focuses on the development and

application of sensitivity tools for better understanding and quantifying the process of cloud formation within global models.

1.1 Aerosols, Clouds, and Climate

Clouds cover roughly half of the Earth and play a central role in the climate system, affecting numerous Earth processes. Microphysical processes such as the formation of cloud hydrometeors can impact the autoconversion of cloud water to rain and snow, strongly influencing important climate features such as liquid and ice water paths and precipitation rates [6]. Because of this clouds can act as effective redistributors of humidity and precipitation, impacting local meteorology, regional atmospheric features, and aqueous and gas phase tropospheric chemistry. At higher altitudes, clouds containing ice crystals can act as a sink for water vapor over regions of deep convection. This controls the flux of heat and water vapor through the tropopause, influencing both tropospheric and stratospheric water content [e.g., 8, 9]. This can have profound impacts on stratospheric ozone chemistry [10], influencing atmospheric features like stratospheric temperature structure [11]. Beyond these effects, clouds also modulate the radiative budget of Earth by scattering solar and terrestrial radiation, which impart cooling and warming influences on Earth respectively. The net of these competing processes is mostly a function of the thermodynamic state (temperature and pressure) of the cloud [12]. Liquid or warm clouds, such as shallow cumulus and stratocumulus, are composed of aqueous droplets and are found in the lowest few kilometers of the atmosphere where temperatures are greater than 0.0 °C. Due to their bright, highly reflective nature, warm clouds typically exert a net cooling effect on the climate as they scatter more solar radiation into space than trap exiting terrestrial radiation. At higher altitudes and colder

temperatures, mixed-phase clouds containing both ice crystals and supercooled aqueous droplets display widely varying radiative properties which strongly depend on the relative amounts of ice and liquid water present. Above six kilometers thin, translucent ice clouds containing diverse ice crystal habits and optical thicknesses reflect only a small portion of solar radiation but absorb exiting infrared radiation efficiently, resulting in a net warming effect globally. Satellite measurements show that small changes to microphysical cloud properties such as cloud hydrometeor effective radius and number concentration can have large impacts on their radiative properties and lifetime [13]. Measurement and modeling studies reveal these radiative effects to be especially important in the tropics, where ice cloud occurrence is highly frequent [e.g., 14, 15].

Liquid and ice cloud hydrometeors form upon pre-existing aerosol particles when threshold environmental supersaturations are reached within a parcel of air. Most often supersaturation generation within the parcel is driven by atmospheric vertical motion which causes expansion cooling, resulting in a decrease in the saturation vapor pressure of water within the forming cloud; this vertical motion can be forced by numerous phenomena ranging from highly localized surface heating or gravity waves to large scale motion at frontal interfaces [16, 17]. Upon nucleation, cloud hydrometeors grow through the transport (condensation or deposition) of water vapor to their surfaces. As their number concentration increases, so does the rate at which water vapor is depleted from the forming cloud. Eventually this water vapor sink overwhelms the source of water vapor from expansion cooling, and a maximum supersaturation is reached within the cloud; the nucleation of additional aerosol particles ceases at this point. Liquid cloud hydrometeors are nucleated when high enough environmental supersaturations are

reached to allow unstable growth upon the deliquesced or immersed aerosol particles. The fraction of particles that participate in this growth and activate into cloud droplets are termed cloud condensation nuclei (CCN). For a given aerosol particle, the supersaturation needed for CCN activation is termed the critical supersaturation which is mostly a function of the chemical composition and size of the aerosol. Once an aerosol particle has activated into a cloud droplet, they deplete water vapor from the forming cloud through condensational growth. Numerous species of aerosol can act as CCN including internal and external mixtures of organics, nitrate, sulfate, sea salt, and other inorganic salts [18]. Measurement and laboratory studies show that insoluble species such as dust and black carbon can also act as CCN through adsorption activation if water molecules are able to adsorb to the surface of the aerosol [19]. Cirrus or ice cloud hydrometeors nucleate through both heterogeneous and homogeneous freezing. Homogeneous freezing occurs within small, aqueous droplets at extremely high supersaturations (> 1.5 with respect to ice at cirrus relevant temperatures) and low temperatures (< -38 °C) [20] while heterogeneous freezing occurs upon insoluble aerosol through multiple modes including: immersion, condensation, deposition, and contact freezing. Various species of insoluble aerosol can initiate heterogeneous freezing including black carbon, organic carbon, dust, and bacteria, Referred to as ice nuclei (IN). This typically happens at much warmer temperatures and lower supersaturations than those needed for homogeneous freezing. The ambient temperature and supersaturation at which insoluble aerosol nucleate ice is a complex function of aerosol characteristics including chemical composition, surface area, and active surface freezing site density [21]. At colder temperatures and moderate relative humidities, glassy aerosol and crystallized salts can act as IN [22, 23]. The

presence of large concentrations of deliquesced aerosol compared to insoluble aerosol and the varying freezing efficiency of the latter implies a wide dynamic range in crystal number concentration and cloud properties when both freezing mechanisms are active [e.g., 24, 9, 25].

Because clouds formation occurs upon atmospheric aerosol particles, it is an especially important process to understand as it is the main mechanism through which human behavior can influence cloud properties. Anthropogenic activities such as combustion and land use changes emit substantial amounts of particles and reactive gasses into the atmosphere which can significantly alter background aerosol concentrations from their natural state.

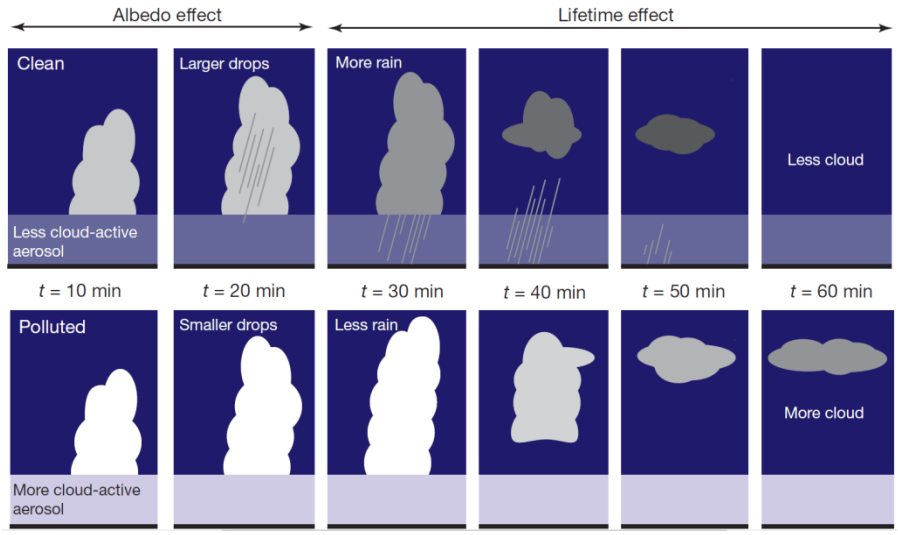

Figure 1: Schematic of the first aerosol indirect effect (albedo effect) and second indirect effect (lifetime effect or Albrecht effect) [1].

Theses aerosol can scatter solar and terrestrial radiation, known as the “aerosol direct effect”. In addition, through changes to CCN and IN concentrations, they can alter properties clouds such as their radiative characteristics (albedo effect) and persistence (lifetime effect) which is known as the “aerosol indirect effect” (Figure 1) [1]. The

aerosol indirect effect is currently the largest source of uncertainty in estimates of anthropogenic effects on the radiative budget of Earth and is estimated to be as large as one third of the current warming experienced from CO_2, although opposite in sign.

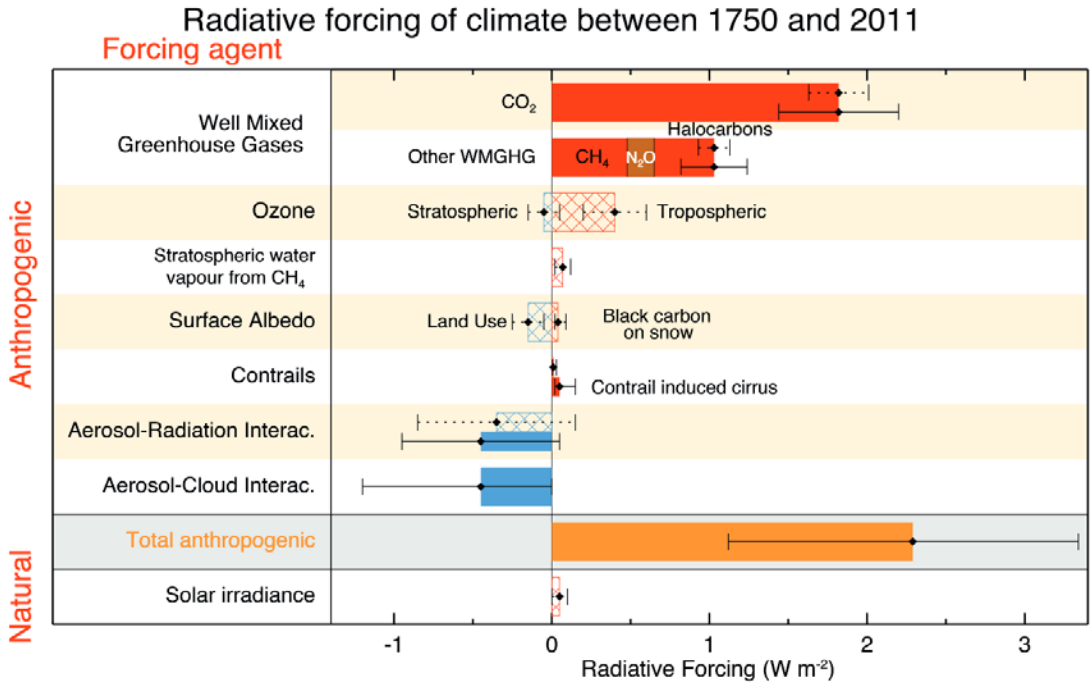

Figure 2: Changes in radiative forcing from pre-industrial to present day as a function of anthropogenic and natural forcing agents [2].

More exactly, the current radiative forcing attributable to the aerosol indirect effect are estimated to be -1.2 Wm^{-2} to 0.0 Wm^{-2} with 95% confidence (Figure 2) [2]. As mentioned, this range arises from many sources such as uncertainty in particulate and reactive gas emissions but is largely driven by uncertainties in the cloud formation process itself. Specifically, understanding cirrus cloud formation on global scales remains a considerable challenge [26, 27, 12, 28, 29] and contributes largely to the current uncertainty in the aerosol indirect effect. To better understand the role of aerosols and

clouds on global scales, large scale models are used where the physics governing cloud formation, persistence, and interactions with solar radiation are explicitly considered.

1.2 Understanding Cirrus Cloud Formation on Global Scales

In the atmosphere, cloud processes occur on spatial and temporal scales spanning orders of magnitude (Figure 3) [3].

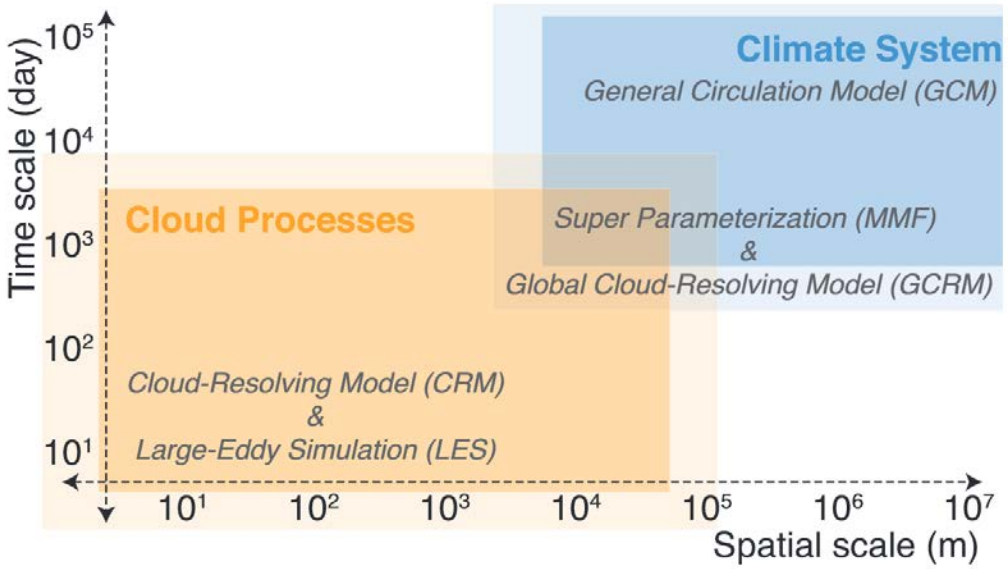

Figure 3: Schematic of the spatial and temporal scales relevant to processes involving clouds and the climate system [3].

For example, stratocumulus decks can extend for hundreds of kilometers and persist for hours while the microphysics governing their formation occurs on length scales of a few micrometers over time periods of only a few minutes. In large scale atmospheric models, spatial and temporal domains must be discretized, typically resulting in resolved spatial and temporal scales that are much larger than those characteristic of microphysical cloud processes. For example, current global climate models possess horizontal domains

discretized to length scales on the order of hundreds of kilometers and are integrated with time steps of minutes. This means that the time-dependent equations governing stratiform cloud formation cannot be integrated explicitly and instead must be parameterized which is achieved through the application of cloud formation parameterizations. These can be physically based (which are functions of physical fields resolved within the model) or numerical fits to offline integrations of the relevant dynamical equations. Physically-based cirrus formation parameterizations [30, 31, 32, 33, 34, 4, 35, 5] link formed crystal number concentration, N_i, to precursor aerosol and other dynamic fields, providing predictions of cloud properties [e.g., 24, 36]. Because of the high degree of interaction between model inputs in parameterizations like these, predicting how modeled cloud state will respond to perturbations in model inputs (the sensitivity of cloud properties to model inputs) and how each model input drives variability in predicted crystal number concentration within a global modeling framework remains challenging.

Studies of aerosol-cloud interactions often focus on the influence of model fields (or process parameterizations) on simulated cloud characteristics (e.g., ice water path, effective radius, and radiative influences). Most often impacts are quantified one variable at a time in sensitivity analyses where whole model integrations are compared after finite perturbations of model variables or parameters are made. For example, Gettelman et al. [37] used two ice formation parameterizations [34, 5] in the CESM Community Atmosphere Model Version 5.1 (CAM 5.1) to assess the importance of the active fraction of black carbon number concentration, the lower size limit of deliquesced sulfate allowed to participate in homogeneous freezing, and the representation of subgrid scale vertical velocity on ice crystal number concentration between present and preindustrial times.

Using the NASA Global Modeling Initiative (GMI) chemical transport model, Barahona et al. [24] investigated the dependence of cirrus formation on both the inclusion and description of heterogeneous ice nucleation within a physically-based ice microphysical parameterization. Individual model integrations for five different heterogeneous freezing spectra revealed differences in predicted ice crystal number concentration by a factor of 20 when averaged globally. The authors demonstrated the strong influence that the treatment of insoluble aerosol (dust and black carbon aerosol) can have on the variability in predicted crystal number concentration; allowing as little as 1% of the simulated black carbon aerosol to participate in heterogeneous freezing caused appreciable effects on crystal number concentration and predicted maximum supersaturations in forming clouds.

Brute force sensitivity analysis is routinely used in studies of warm/mixed phase clouds as well. For example, Spracklen et al. [38] used the GLObal Model of Aerosol Processes model (GLOMAP) to show that uncertainties in cloud microphysical processes were responsible for larger uncertainties in modeled cloud condensation nuclei (CCN) concentrations than uncertainties in modeled SO_2 emissions. This analysis was carried out by investigating the effect of individually perturbing microphysical parameters in offline simulations. Sotiropoulou et al. [39] used in-situ measurements of aerosol and CCN number and the GISS GCM Model II' to quantify the uncertainty introduced to autoconversion and radiative forcing estimates from the application of Köhler theory which is used for computing CCN number concentrations. The sensitivity of the uncertainties to parameters that influence cloud droplet formation was assessed by making numerous additional global model simulations for a range of updraft velocities and the water vapor uptake coefficients. Alternatively, with an emulated version of the

GLOMAP model, Lee et al. [40] analyzed the influence of model parameters on CCN uncertainty. Here, Gaussian process emulation was used to perform a variance-based sensitivity analysis over multiple model parameters, providing their spatial contribution to CCN uncertainty. In order to develop emulated models like these, many individual model simulations are required to capture the dependence of CCN on parameters across their wide ranges of values.

Although these approaches are conceptually straightforward, they require a large number of model simulations and come at significant computational cost. Furthermore, finite difference approximations to model tendencies may be subject to error given the non-linear nature of some model parameterizations. These issues can be addressed through the development and application of direct sensitivity tools developed from the original parameterization codes. These tools provide analytically accurate sensitivities of specific model outputs to a range of inputs parameters at computational costs comparable to a small multiple of the original parameterizations with utility in a wide array of applications. Direct sensitivity tools have recently been used to analyze warm cloud microphysical processes in global model simulations. Karydis et al. [41] developed the adjoint model of the Kumar et al. [42] warm cloud activation parameterization and used output from the NASA GMI and GEOS-Chem chemical transport models (CTM) to quantify the sensitivity of formed cloud droplet number concentration, N_d, to the water uptake coefficient, updraft velocity, hygroscopicity, and aerosol number concentration and size. This sensitivity information was extended to understand what causes differences in warm cloud indirect forcing estimates within these two global models when using the this activation parameterization. Using the sensitivity fields derived by Karydis et al. [41]

from the GMI simulations, Moore et al. [43] related uncertainties associated with the prediction of CCN concentrations to uncertainties in global N_d and aerosol indirect forcing. It was found that the importance of CCN prediction error is highly dependent on background aerosol concentrations; in continental or polluted regions, uncertainties in CCN concentrations result in roughly 10% N_d uncertainty, whereas in pristine or remote regions, this was as high as 70%. Morales and Nenes [44, 45] used adjoint sensitivity fields to identify which process level variables and parameterization characteristics caused differences in predictions of N_d and aerosol indirect effect estimates in CAM 5.1. The focus was to understand the cause of discrepancies between the Abdul-Razzak and Ghan [46] and Fountoukis and Nenes [47] warm cloud activation parameterizations within CAM 5.1. Here discrepancies were driven by the treatment of water uptake by coarse mode particles and the sensitivity of each parameterization to accumulation mode geometric mean diameter. The former drove discrepancies in N_d in pristine marine environments, while the latter affected N_d and cloud properties in polluted regions throughout the globe.

Direct sensitivity tools of cloud activation schemes have important applications beyond those related to process and parameterization studies. Saide et al. [48] used the adjoint model of a stratiform cloud activation parameterization within a three-dimensional variational data assimilation framework to obtain estimates of below-cloud aerosol characteristics by optimizing agreement between simulated and observed column droplet number concentrations. Coupling the droplet activation parameterization adjoint of Kumar et al. [42] with the adjoint model of GEOS-Chem, Karydis et al. [49] studied the role of global aerosol emissions on N_d and cloud albedo in three regions of the US

and Europe. The authors determined that N_d over the eastern United States is most sensitive to SO_2 emissions in the summer and NH_3 emissions during winter. Using the adjoint sensitivities as a reduced form model, they found that cloud albedo could change by as much as 42% by year 2050 over parts of central Europe in response to estimated emission changes.

1.3 Thesis Outline

Until this point, direct sensitivity tools for investigating aerosol-ice cloud interactions have not been developed, despite their applications in inverse modeling, optimal parameter estimation, and model evaluation. Here we present the development of the adjoint model of the Barahona and Nenes stratiform cirrus formation parameterization [4, 35, 5] (BN09) and its implementation in CAM 5.1. A brief overview of BN09 is presented followed by a detailed discussion of the development of its adjoint model (ABN09). A description of the CAM 5.1 simulations with ABN09 is presented followed by a discussion of the global distribution of formed ice crystal number concentration sensitivities to aerosol and dynamical model fields. The utility of the sensitivity information provided by ABN09 is then extended by quantifying the extent to which the variability in simulated formed crystal number concentration is influenced by an array of model input fields.

CHAPTER 2

DEVELOPING DIRECT SENSITIVITY TOOLS FOR INVESTIGATING ICE NUCLEATION IN ATMOSPHERIC MODELS

2.1 The Cirrus Formation Parameterization Used in This Work

The adjoint model is based on the cirrus formation parameterization of Barahona and Nenes [4, 35, 5]. This physically-based scheme provides a pseudo-analytical solution to an ascending, zero-dimensional cloud parcel representation of stratiform cirrus cloud formation; the equations from which formed crystal number concentration, N_i, is computed are based on the conservation of mass and energy considering active mass transfer between hydrometeors within a parcel of air rising at a constant velocity. Ice crystals are formed within and upon preexisting soluble and insoluble aerosol respectively, and grow by the deposition of water vapor during cloud formation. The formulation of BN09 is unique as it permits the use of any heterogeneous ice nucleation spectrum, F_{IN}, (i.e., the function that computes the number of crystals that freeze heterogeneously based on environmental supersaturation and insoluble aerosol characteristics). F_{IN} depends on the modes of heterogeneous freezing considered and on insoluble aerosol size, number, and type. Here we use the empirically-derived heterogeneous freezing spectrum of Phillips et al. [50] (PDA 2008) owing to its explicit consideration of multiple aerosol types and several modes of heterogeneous freezing. In BN09, N_i is computed by determining the contribution of both homogeneous freezing, $N_{i,hom}$, and from heterogeneous freezing, $N_{i,het}$, to N_i which is achieved in three conceptual steps. In the first step, the limiting number of IN needed to inhibit homogeneous freezing, N_{lim}, is determined by computing the number of IN required to depress the maximum

supersaturation of the parcel to the supersaturation threshold needed for homogeneous freezing, S_{hom}, (e.g., [20, 51]). Next, F_{IN} is evaluated at S_{hom} to compute $N_{i,het}(S_{hom})$. In the second step, if $N_{i,het}(S_{hom}) > N_{lim}$, homogeneous freezing is inhibited completely and N_i is computed by evaluating $F_{IN}(S_{max})$. S_{max} is then solved for iteratively using the bisection method from the balance of supersaturation production by expansion cooling within the parcel and supersaturation depletion by the depositional growth ice crystals (Equation 1).

$$F_{IN}(S_{max}) - \frac{N^*(1+S_{max})e^{\frac{2}{\lambda S_{max}}}}{\sqrt{\Delta S_{char}}} = 0 \qquad (1)$$

N^* is the ratio of the rate change of supersaturation from expansion cooling to the time rate change of surface area of the crystal population, ΔS_{char} is the difference between S_{max} and the characteristic freezing supersaturation of the IN population, λ is a supersaturation generation term dependent on temperature and ice properties, and T is the temperature [5]. In the third step, if $N_{lim} > N_{i,het}(S_{hom})$, both homogeneous and heterogeneous freezing contribute to N_i, the maximum supersaturation of the parcel is set to S_{hom}, and N_i is computed by the homogeneous freezing parameterization of [4], augmented to consider the influence of IN on S_{max} [35, 5].

$$f_c = \frac{\rho_a}{\rho_i}\frac{[k(T)]^{\frac{1}{2}}}{\beta N_o}\left[2\alpha w\frac{(S_{hom}+1)}{\pi\bar{\Gamma}S_{hom}}\right]^{\frac{3}{2}}\left[1-\left[\frac{F_{IN}(S_{hom})}{N_{lim}}\right]^{\frac{3}{2}}\right]^{\frac{3}{2}} \qquad (2)$$

$$N_{i,hom} = N_o\, e^{-f_c}(1-e^{-f_c}) \qquad (3)$$

f_c is the fraction of soluble aerosol that freeze, $k(T)$ is a temperature dependent parameter that relates the nucleation rate of ice germs to supersaturation, T is the temperature, β is a parameter related to the influence of vapor deposition on supersaturation depletion, N_o is the number concentration of supercooled droplets (here deliquesced sulfate aerosol), α is a parameter related to the influence of updraft velocity on supersaturation generation, w is the cloud forming updraft velocity, and $\overline{\Gamma}$ is the effective crystal growth parameter. To summarize, for both regimes of crystal production, N_i is given by:

$$N_i = \begin{cases} N_{i,hom} + N_{i,het}(S_{hom}); & N_{i,het}(S_{hom}) < N_{lim} \quad S_{max} = S_{hom} \\ N_{i,het}(S_{max}); & N_{i,het}(S_{hom}) > N_{lim} \quad S_{max} < S_{hom} \end{cases} \tag{4}$$

An important detail of BN09 is how N_i responds to changes in the number of insoluble aerosol acting as IN for fixed temperature, updraft velocity, pressure, soluble aerosol characteristics, and insoluble aerosol size, which is shown in Figure 4.

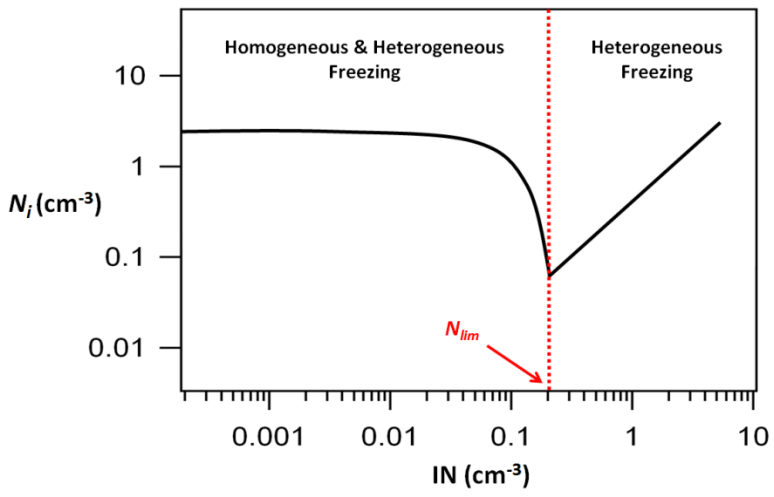

Figure 4: Schematic of the transition between combined homogeneous/heterogeneous freezing and pure heterogeneous freezing as a function of only insoluble aerosol number concentration.

At low IN number concentrations, ice crystals are formed through both homogeneous and heterogeneous freezing. As the IN number concentration increases, N_i starts to decrease due to the inhibition of homogeneous freezing. The extent of this inhibition increases as you move closer to the point where the number concentration of IN equal N_{lim}, marked by the red, dashed line running vertically in Figure 4. As you move to IN number concentrations higher than N_{lim}, homogeneous freezing is completely inhibited and any increases in IN number concentration increase N_i through changes to only $N_{i,het}$. Because the number concentrations of soluble aerosol tend to be orders of magnitude larger than that of insoluble aerosol, when homogeneous freezing occurs, N_i is typically much higher than when freezing is purely heterogeneous.

2.2 The Heterogeneous Freezing Spectrum Used in This Work

PDA 2008 [50] is an empirically-derived description of heterogeneous freezing that relates chemical composition and size of several types of insoluble aerosol to its ability to serve as an IN (freeze heterogeneously) in the immersion and deposition nucleation modes. Three main types of aerosol are considered including dust and metallic compounds, inorganic black carbon, and organic carbon, which make up more than 75% of IN globally (e.g., [50, 52]). The use of PDA 2008 implies F_{IN} takes the form of Equation 5, where the number of insoluble aerosol that freeze heterogeneously of aerosol species *i* is computed by integrating the size distribution, $dN_{IN,i}/dlogD_i$, of species *i* times a cumulative exponential distribution over all sizes above a minimum diameter, $D_{min,i}$. This is performed for all insoluble aerosol species by summing over *i*.

$$F_{IN} = \sum_{i} \int_{\log(D_{min,i})}^{\infty} \{1 - e^{-\mu_i(D_i, S_i, T)}\} \frac{dN_{IN,i}}{dlogD_i} dlogD_i \quad (5)$$

μ_i represents the number of ice embryos per insoluble aerosol particle in group i, D_i is the diameter of aerosol in group i, S_i is the environmental supersaturation with respect to ice, and T is the temperature.

2.3 Adjoint Model Development and Testing

The gradient model of BN09 was developed using the automatic differentiation software TAPENADE V3.5 [53]. With this tool, the chain rule is systematically applied to the BN09 parameterization algorithm, producing either the adjoint model or tangent linear model (TLM) of BN09. When the number of independent model variables is less than the number of dependent model variables, using the TLM method is advantageous over the adjoint method, as fewer operations are required to provide partial derivatives of the model output with respect to each model input. The opposite holds when models contain more inputs than outputs (such as BN09), hence the adjoint method is used here.

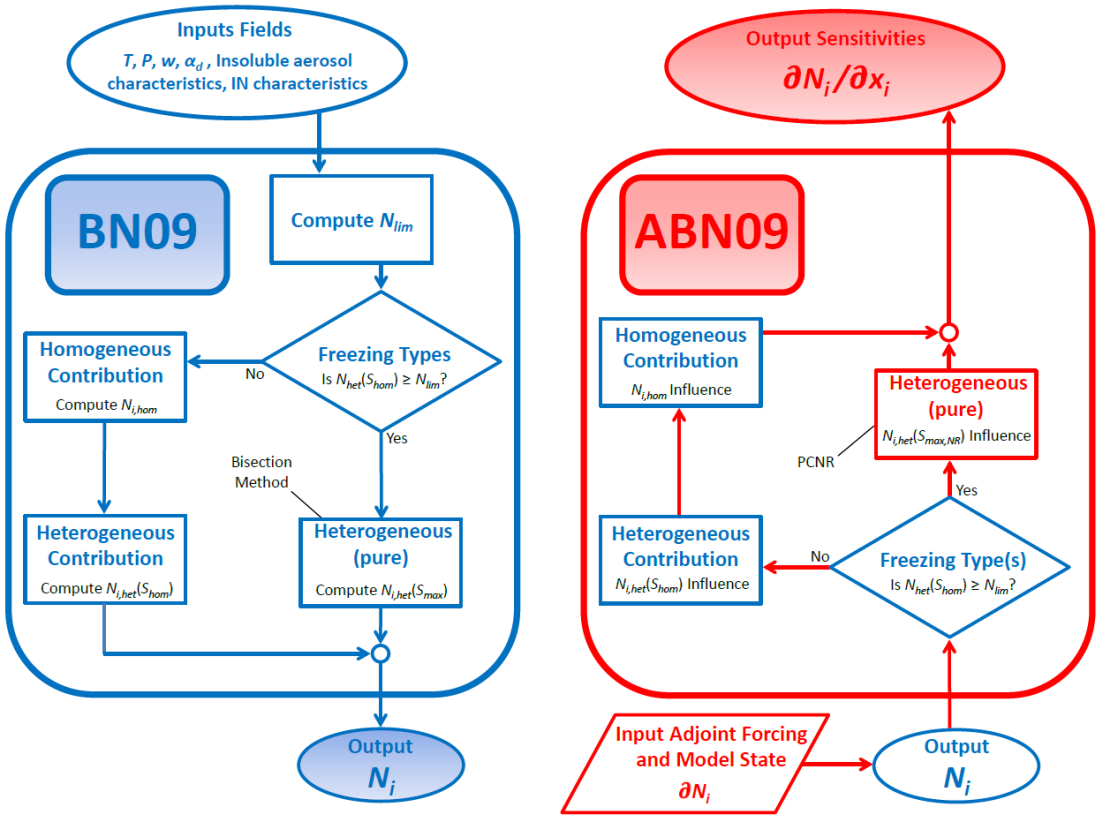

Figure 5: Call tree of the cirrus formation parameterization used in this work (blue) and the adjoint model of the parameterization used in this work (red). Outputs from both models are shown in the shaded boxes.

Figure 5 shows a comparison of the call trees of BN09 (left, blue box) and ABN09 (right, red box) with the outputs of both models shown in shaded boxes. Sensitivity information is provided by first making a single call to BN09 to evaluate the state of all variables used in BN09 followed by a call to ABN09; the sensitivity of N_i to all input fields is determined by propagating an adjoint forcing in N_i, ∂N_i, backward through the call tree of BN09 to retrieve the differential in parameterization inputs, ∂x_i, where x_i is any of the inputs to BN09. Adjoint sensitivities are then expressed as first order derivatives, $\partial N_i/\partial x_i$.

The use of the bisection method to iteratively solve Equation 1 for S_{max} inhibits the propagation of the chain rule of differential calculus through BN09 as no functional

relationship between inputs and outputs exists across this step. To alleviate this issue, the post-convergence Newton-Raphson (PCNR) method is applied [54, 55]. Here the bisection method of BN09 is replaced with an explicit expression for S_{max} derived from the Newton-Raphson method, using the maximum supersaturation predicted from the bisection method, S^*_{max}, as the point about which the first order expansion is made (Equation 6). With this, the maximum supersaturation of the parcel is expressed as $S_{max,NR}$.

$$S_{max,NR} = S^*_{max} - \frac{f(S^*_{max})}{\left.\frac{\partial f(S_{max})}{\partial S_{max}}\right|_{S^*_{max}}} \qquad (6)$$

$f(S^*_{max})$ corresponds to the LHS of Equation 1. $\partial f(S_{max})/\partial S_{max}$ is obtained from the TLM of BN09 (also developed using TAPENADE), evaluated at S^*_{max}. The advantage of PCNR is that an explicit functional relationship between S_{max} and the rest of the parameterization is obtained without redeveloping the original parameterization. PCNR has been used successfully to address the differentiation of non-continuous sections of complex aerosol thermodynamic code [55] and stratiform droplet activation code [41].

ABN09 was constructed to compute the gradient of N_i with respect to updraft velocity, w; number concentration of: deliquesced sulfate, N_{sulf}, accumulation mode dust, $N_{dust,a}$, coarse mode dust, $N_{dust,c}$, accumulation mode black carbon, N_{bc}, and accumulation mode organic carbon, N_{org}; geometric mean diameter of: sulfate, D_{sulf}, accumulation mode dust, $D_{dust,a}$, coarse mode dust, $D_{dust,c}$, accumulation mode black carbon, D_{bc}, and accumulation mode organic carbon, D_{org}; and temperature, T. The adjoint also computes

the sensitivity of N_i to the water vapor deposition coefficient, α_d, which modifies the rate of water vapor transport to frozen ice crystals due to non-continuum effects.

The accuracy of the adjoint sensitivities computed from ABN09 were assessed against sensitivities from centered finite differences approximations to first order derivatives computed from BN09 at atmospherically relevant climate states using offline GEOS-5 [56] cloud forming updraft velocity and aerosol fields from the Goddard Chemistry Aerosol Radiation and Transport (GOCART) model. This was achieved by making a present day, single year global model integration with GEOS-5 where the fields needed to drive ABN09 were annually averaged within each GCM grid box. Sea surface temperatures were set to present day values and aerosol species including sulfate, dust, black carbon, and organic carbon were considered (typical ranges for the values of all independent model fields are presented in Table 1).

Table 1: GEOS-5 adjoint and finite difference sensitivity comparison

Field	w	α_d	N_{sulf}	D_{sulf}	T	N_{bc}	D_{bc}	N_{org}	D_{org}	N_{dust}	D_{dust}
Range	0-1 (ms^{-1})	0.1-1.0	0-25 (cm^{-3})	0.02-0.05 (μm)	195-235 (K)	0-0.5 (cm^{-3})	0.1-0.2 (μm)	0-200 (cm^{-3})	0.1-0.2 (μm)	0-0.3 (cm^{-3})	1.0-1.5 (μm)
Average Relative Error	0.01	0.01	0	1.3×10^{-6}	0.03	0.01	8.9×10^{-4}	0.02	0.02	4.0×10^{-4}	2.8×10^{-4}

The sensitivity comparison was performed at the 200 hPa pressure level with temperatures less than 235 K globally, ensuring no mixed-phase crystal production. Finite difference perturbations of +/- 0.01% about the mean state were used for all model variables. Presented in Table 1, finite difference sensitivities are in excellent agreement

with adjoint sensitivities for all model variables, with the average relative error equal to 0.92%; relative error is defined as the absolute value of the difference between adjoint sensitivities and finite different sensitivities divided by finite difference sensitivities.

CHAPTER 3

DISTRIBUTION OF ICE CRYSTAL NUMBER SENSITIVITIES WITHIN A GLOBAL CLIMATE MODEL

3.1 Description of NCAR's CAM 5.1 Global Climate Model and Model Integrations

The spatial distribution of crystal number sensitivity to the model fields outlined in Chapter 2.3 was computed using ABN09 within CAM 5.1 [57, 45]. Simulations were made with present day sea surface temperatures and greenhouse gas mixing ratios and consisted of a two year spin up followed by single year integration with a 30 min time step and 2.50×1.88 degree resolution. Surface emissions of reactive gases and aerosols were provided by the emissions inventory of Lamarque et al. [58]. Aerosol particles were modeled using the MAM3 model [59], with three, internally mixed lognormal modes (Aitken, accumulation, and coarse). Geometric standard deviations of the three modes was fixed and used along with total aerosol mass and total aerosol number concentration to constrain the geometric mean diameter of each mode throughout the model integration. The number concentration of soluble and insoluble aerosol species in a given mode was determined by scaling the total aerosol number in a given mode by the mass fraction of that species in that mode [45]. The two-moment bulk microphysical scheme of Morrison and Gettelman [60] was used to describe the time evolution of ice and liquid water hydrometeor number and mass mixing ratio for stratiform clouds; in this scheme, the source of nucleated ice crystals is computed using BN09 containing PDA 2008.

ABN09 was driven using CAM 5.1 sulfate number concentration and geometric mean diameter from the Aitken mode as representative soluble aerosol. Insoluble aerosol

consisted of dust in the accumulation and coarse mode, accumulation mode black carbon number, and accumulation mode primary organic carbon. Here we assumed that primary organic carbon is the most representative of insoluble organic carbon as secondary organic carbon tends to be much more oxidized and water soluble, meaning it is likely to serve as a CCN and be removed through the autoconversion of cloud water to rain water. A complete outline of the aerosol characteristics used in the CAM 5.1 simulations can be seen in Table 2.

Table 2: Aerosol characteristics from CAM 5.1 integrations

Species	Size Modes	Aerosol Number Scaled by:	Number Concentration (cm^{-3})	μ_g (μm)	σ_g
Sulfate	Aitken	Mass fraction in Aitken	20.0-950.0	0.02-0.04	2.3
Black Carbon	Accumulation	Mass fraction in accumulation	0.0-9.0	0.1-0.2	1.8
Organic Carbon	Accumulation	Mass fraction in accumulation	10.0-150.0	0.1-0.2	1.8
Dust	Accumulation	Mass fraction in accumulation	0.0-35.0	0.1-0.2	1.8
Dust	Coarse	Mass fraction in coarse	0.0-0.23	1.0-1.5	1.6

3.2 Ice Formation in CAM 5.1

The annual average results of the CAM 5.1 simulations and relevant cloud formation driving fields are presented in Figure 6, Figure 7, and Figure 8 at the pressure level of 232.6 hPa, corresponding to the lowest altitude where cirrus ice clouds were observed at every time step of the global model integration (determined from the criterion that $T < 235$ K).

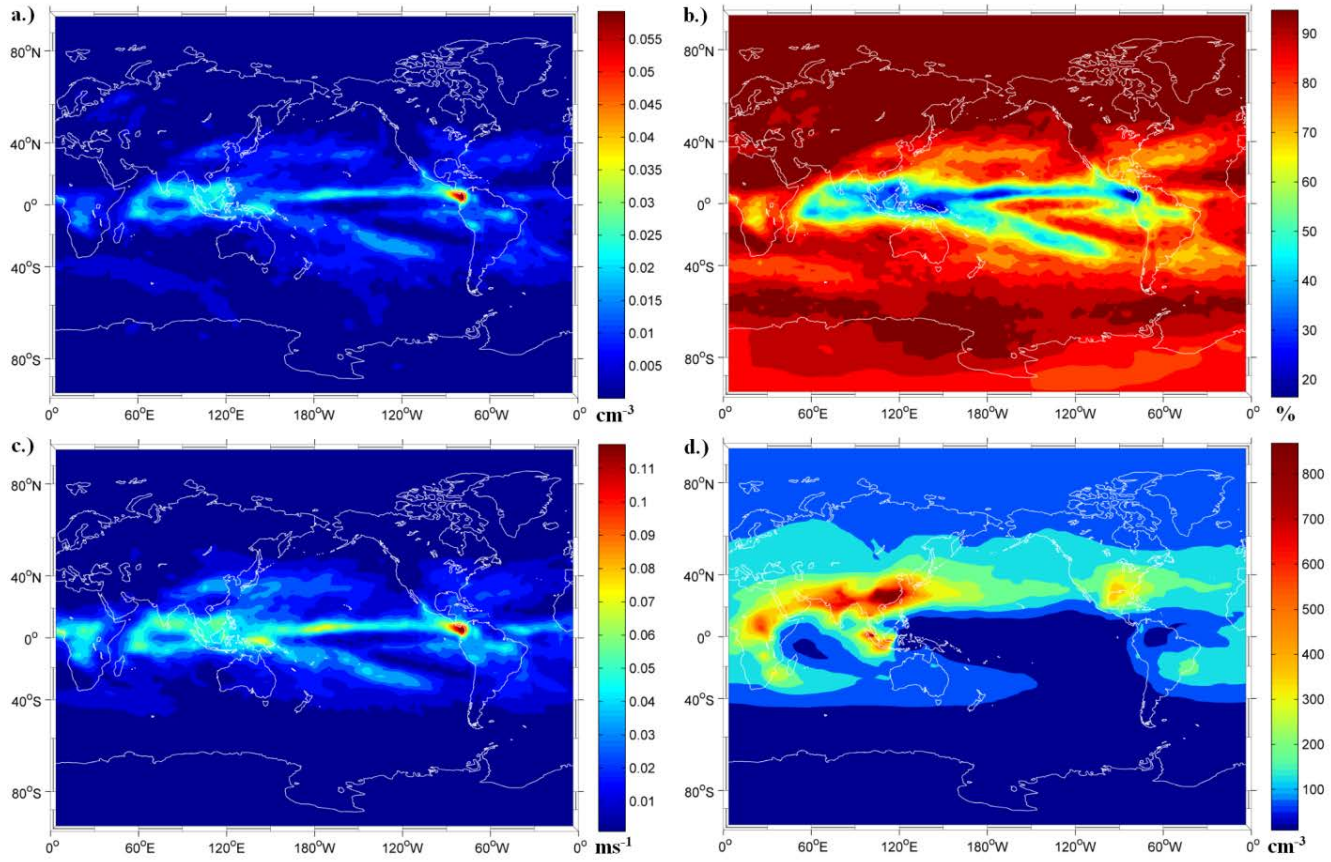

Figure 6: Annually averaged CAM 5.1 cloud formation fields; a.) Formed crystal number concentration (cm^{-3}), b.) Heterogeneous freezing percentage, c.) Updraft velocity (ms^{-1}), d.) Sulfate number concentration (cm^{-3}).

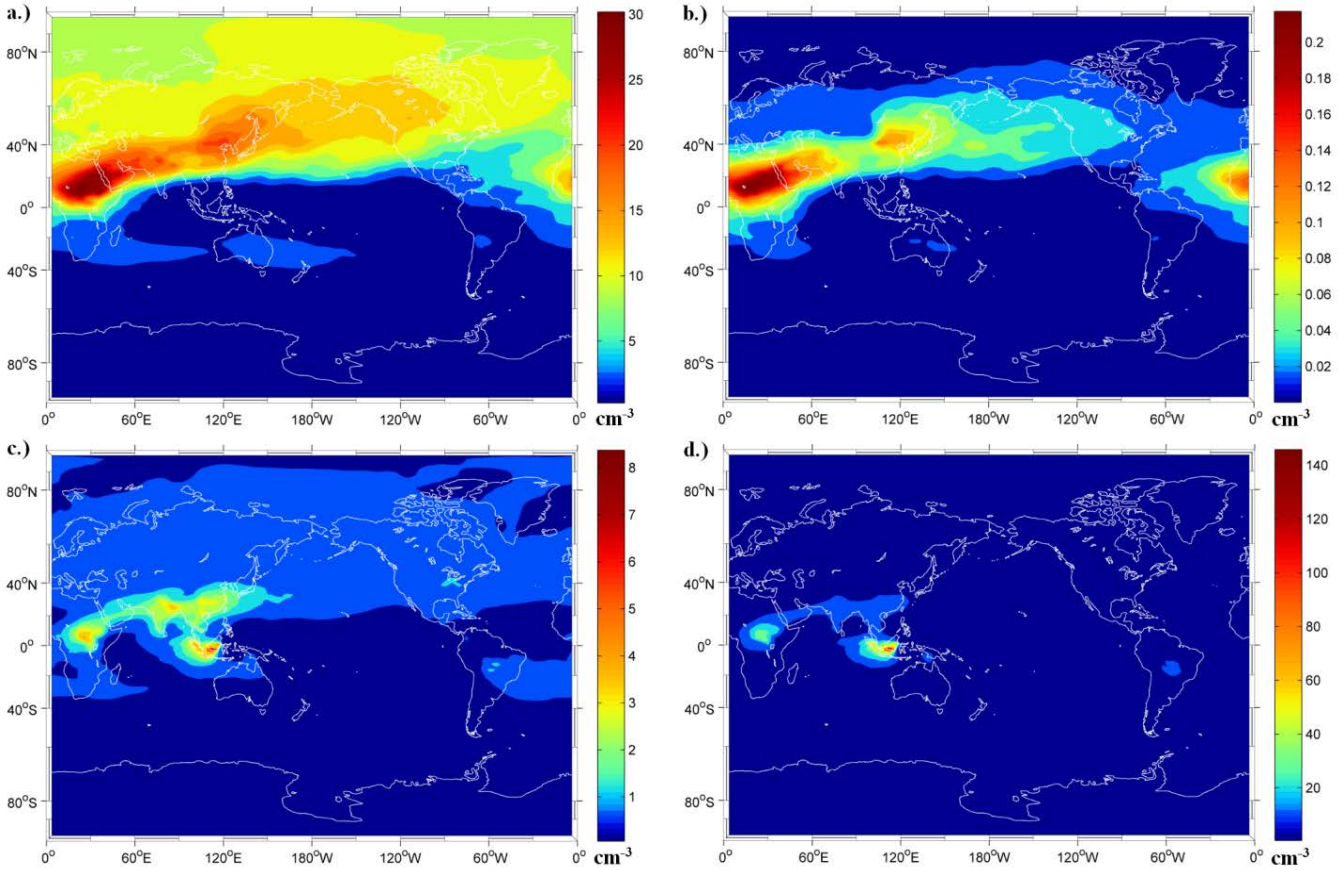

Figure 7: Annually averaged CAM 5.1 cloud formation fields; a.) Accumulation mode dust number concentration (cm^{-3}), b.) Coarse mode dust number concentration (cm^{-3}), c.) Black carbon number concentration (cm^{-3}), d.) Organic carbon number concentration (cm^{-3}).

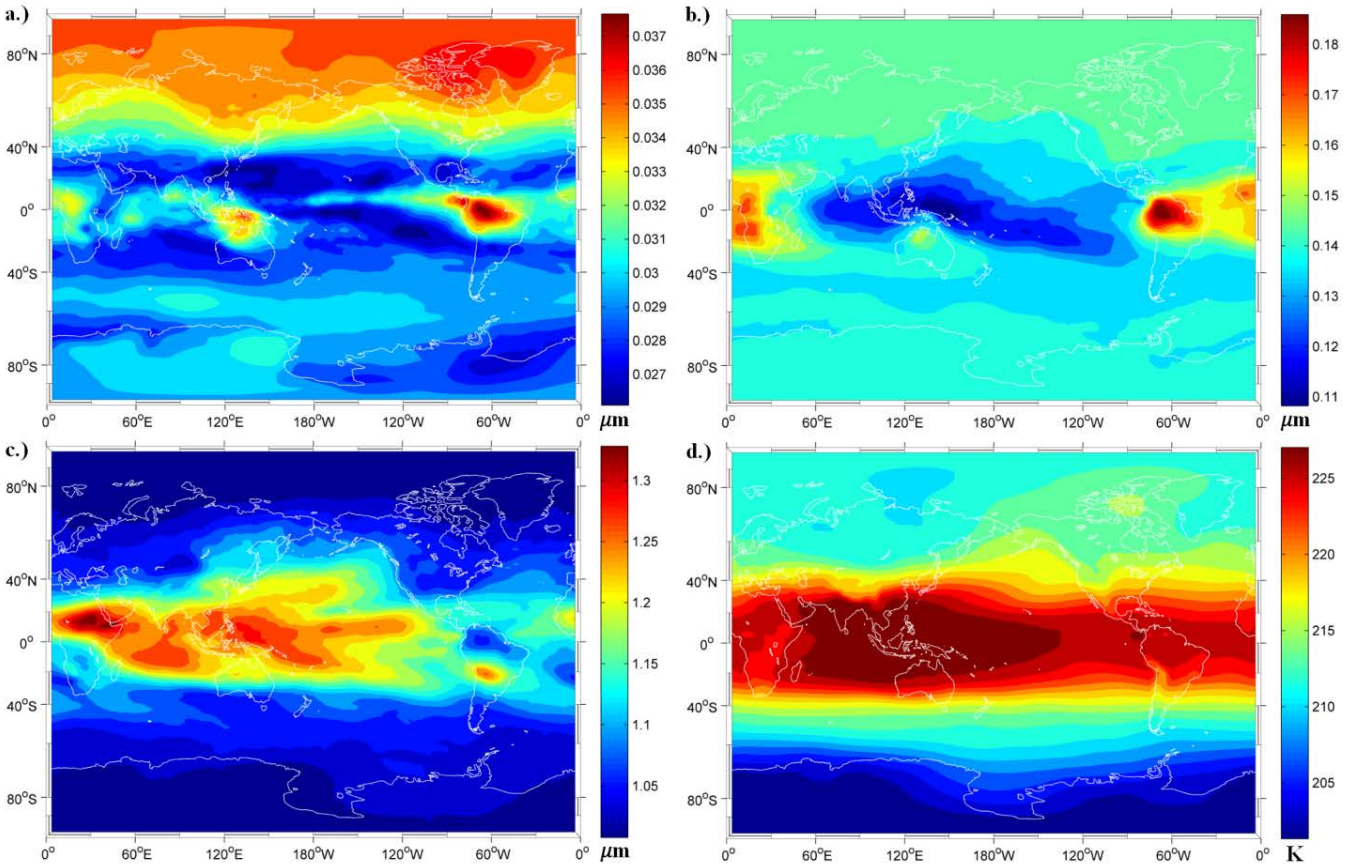

Figure 8: Annually averaged CAM 5.1 cloud formation fields; a.) Aitken mode geometric mean diameter (μm), b.) Accumulation mode geometric mean diameter (μm), c.) Coarse mode geometric mean diamter (μm), d.) Temperature (K).

Figure 6a shows N_i predicted by BN09. The calculation of N_i is not limited to only the locations where cirrus form in CAM 5.1, meaning Figure 6a represents the maximum potential influence of aerosol and dynamical fields on N_i. In the future, fractional cloud occurrence should be considered in studies that use BN09 and ABN09 to scale the magnitude of sensitivities across regions with different cirrus prevalence.

N_i is highest (up to 0.058 cm^{-3}) over the tropics where deep convection and strong surface heating result in stronger atmospheric turbulence and higher scales of cloud forming vertical motion. This allows higher supersaturations to be reached and strong contributions to N_i from homogeneous freezing. In CAM 5.1 the cloud forming updraft

velocity (Figure 6c) is computed as $w = \sqrt{\frac{2}{3}\text{TKE}}$, where TKE is the local kinetic energy associated with turbulent dissipation. Throughout the sub-tropics and mid-latitudes, N_i decreases to approximately 0.015 cm^{-3} and to 0.005 cm^{-3} respectively and is highly correlated with w. This strong spatial correlation illustrates the important influence w has on N_i and suggest that w is the primary controller of N_i. Despite the strength of this correlation, it can be modulated by insoluble aerosol number concentration, especially from dust and black carbon. This can be seen geographically in Figure 6a and 6c over regions such as Central Africa. Here updraft velocities on the order of 0.05 ms^{-1} provide the potential for large supersaturation development and large formed crystal number concentrations. Despite this, N_i is only equal to about 0.008 cm^{-3} whereas in other regions with similar updraft scales and lower insoluble aerosol number concentration such as over the Eastern Indian Ocean, N_i reaches values an order of magnitude larger (0.025 cm^{-3}). This difference in N_i is a result of moderate dust and black carbon concentrations in this region which act to shut down supersaturation development, significantly reducing the contribution of homogeneous freezing to N_i and N_i overall.

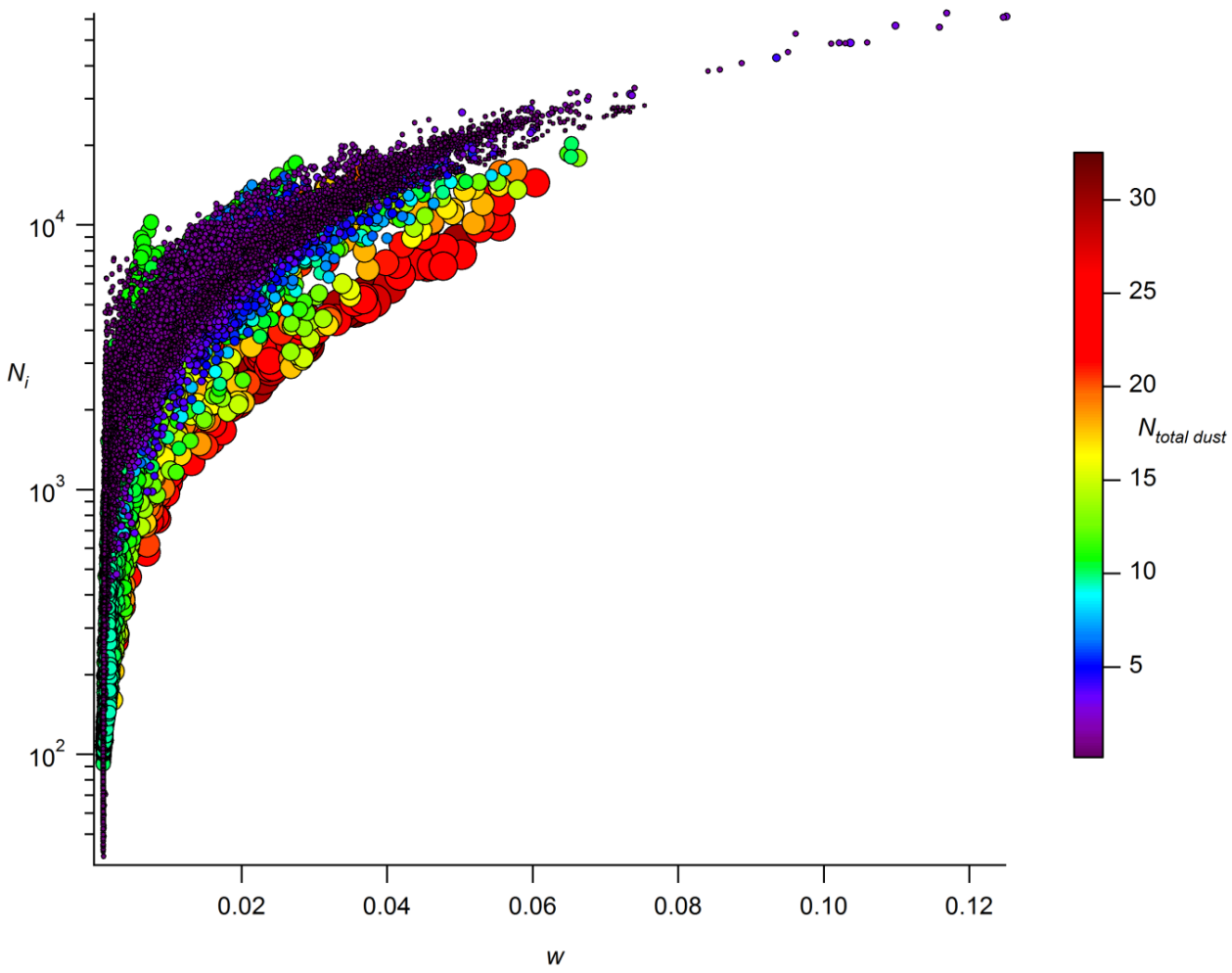

Figure 9: Global annually averaged CAM 5.1 formed crystal number concentration (cm^{-3}) vs. updraft velocity (ms^{-1}). Points are colored and sized by the sum of the accumulation and coarse mode dust number concentration (cm^{-3}).

This influence from insoluble aerosol number concentration on N_i occurs globally and is further illustrated in Figure 9. Here N_i is plotted against w with points colored and sized by the sum of $N_{dust,a}$ and $N_{dust,c}$. A strong correlation between w and N_i across all values of updraft can be seen by the tight grouping of small, purple dots. Over regions of large dust concentrations (greater than 10 cm^{-3}), the strength of this correlation weakens, shown by the large, warm colored points deviating from the main trend. This suggests insoluble aerosol number concentration plays an important secondary role (to updraft velocity) in

modulating N_i and potentially N_i variability in regions where adequate updraft cooling is provided (e.g., the Northern Pacific Ocean and over parts of North Africa).

A more detailed analysis of the influence of insoluble aerosol number concentration on N_i can be seen in the fraction of N_i that originates from heterogeneously frozen crystals (Figure 6b); here three distinct regions can be observed. The first is over regions of high dust and black carbon number concentrations, collocated with weak updrafts (e.g., Eastern Sahara, Western China, and in the Northern Hemisphere north of 40 N). Here dust number concentrations approach 30 cm^{-3} and 0.2 cm^{-3} in the accumulation and coarse mode respectively. Because of the colocation of high insoluble aerosol concentrations and weak updrafts (< 0.01 ms^{-1}), S_{max} is depressed well below the homogeneous freezing threshold, homogeneous freezing contributes little to N_i, and heterogeneous freezing percentages are greater than 95% annually. This is true despite the fact that these regions contain the highest concentrations of sulfate globally. In these regions, insoluble aerosol mostly originate from dust and black carbon making up ~75% and ~5% of the total IN respectively, consistent with in-situ measurements of ice crystal residues [52]. The second region of insoluble aerosol influence on N_i occurs throughout the entire Southern Hemisphere at latitudes below 35 S. Characteristic of this region is low to moderate updraft velocities and concentrations of insoluble aerosol that are the lowest globally. Here heterogeneous freezing dominates crystal production (although to a lesser extent than in the NH), but the absence of insoluble aerosol allows more homogeneous freezing than in the Northern Hemisphere with heterogeneous freezing percentages equal to ~75%. The contribution of heterogeneous freezing to N_i is weakest in regions of low insoluble aerosol concentrations and large updraft velocities where

heterogeneous freezing percentages range from 15% to 50%. These regions, which constitute the third freezing region, are characterized by S_{max} values that frequently reach S_{hom} and are confined to the equatorial Pacific Ocean along the Intertropical Convergence Zone. Because of the large supersaturations and significant contribution of homogeneous freezing to N_i, formed crystal number concentrations are the largest globally (0.025 to 0.058 cm^{-3}) over these regimes. To summarize, N_i scales are similar in the Northern Hemisphere and Southern Hemisphere but for different reasons. In the Northern Hemisphere, large insoluble aerosol number concentrations add weakly to N_i through N_{het} but shut down homogeneous crystal generation, resulting in low predictions of N_i. This is an important point as sulfate concentrations are highest in the Northern Hemisphere meaning the potential for forming ice crystals homogeneously is high and with small variations in insoluble aerosol number, large variability in N_i may be observed. In the Southern Hemisphere low insoluble aerosol number forces less ice to be formed heterogeneously when compared to the Northern Hemisphere. Because of this, homogeneous freezing is less inhibited, resulting in similar values of N_i when compared to the Northern Hemisphere. In the tropics, large updraft velocities and relatively low insoluble aerosol concentrations allow maximum supersaturations to frequently reach the homogeneous threshold, resulting in large contributions of homogeneous freezing to N_i and the highest formed crystal number concentrations globally.

3.3 Global Distributions of Ice Crystal Number Sensitivities

Following is the presentation and analysis of the global sensitivities of N_i to the model fields presented in Chapter 2.3. Sensitivities were computed within CAM5.1 using

ABN09 at the same pressure level as the CAM 5.1 fields presented Figure 6, Figure 7, and Figure 8 and are not weighted by fractional cloud occurrence.

3.3.1 Updraft Velocity

Depending on the dominant freezing mechanism (homogeneous or heterogeneous), the dependence of N_i on w can follow one of two trends (Equation 4). First, when homogeneous freezing is completely inhibited, N_i is related to w only through the influence of w on S_{max}, resulting in changes to $N_{i,het}$. Increases to w causes S_{max} to reach higher values, allowing more of the sparse population of insoluble aerosol to serve as IN. Because of the small number concentrations of insoluble aerosol compared to deliquesced aerosol, significant changes in w have a relatively weak influence on N_i [24] as only insoluble aerosol can contribute to additional crystal production. Alternatively, over regions where homogeneous freezing is the dominant mode of freezing (low heterogeneous freezing percentages), the sensitivity of N_i to w is much stronger, owing to both the relatively populous soluble aerosol concentrations and strong dependence of the fraction of soluble aerosol that freeze (f_c) on w. For typical cirrus formation conditions, f_c exhibits a power law dependence on w ($f_c = aw^b$ from Equations 3 and 4, where b > 1, [5]), meaning that changes in w influence f_c strongly. In Equation 3, N_{sulf} acts as a linear scaling factor to the exponential term containing f_c, meaning N_{sulf} has the potential to strongly modify the dependence of N_i on w when f_c is above 0.1. This dependence is physically consistent with the freezing of a real population of droplets as the number of soluble aerosol that freeze scales with the cumulative probability of freezing of the aerosol population [e.g., 6, 4].

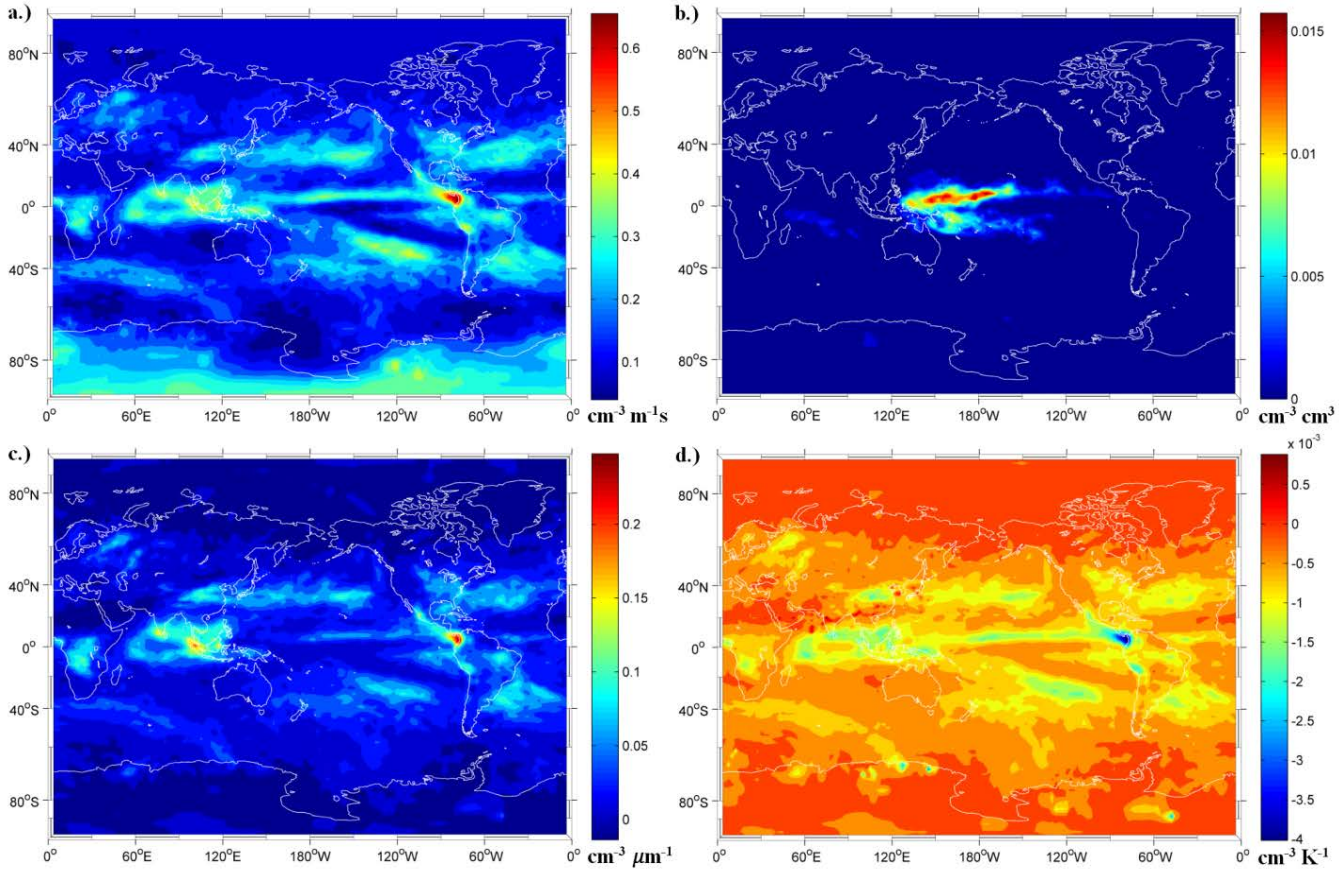

Figure 10: Annually averaged CAM 5.1 cloud formation sensitivities; a.) Updraft velocity (cm^{-3} $m^{-1}s$), b.) Sulfate number concentration (cm^{-3} cm^{3}), c.) Sulfate geometric mean diameter (cm^{-3} μm^{-1}), d.) Temperature (cm^{-3} K^{-1}).

Figure 10a depicts the annual average global distribution of $\partial N_i/\partial w$ where the details discussed in the previous paragraph can be observed. Over the high latitudes of the Northern Hemisphere where dust and black carbon concentrations and heterogeneous freezing percentages are high and w is low, sensitivities of N_i to w are low (~0.1 cm^{-3} $m^{-1}s$). Over the Northern Hemisphere Pacific Ocean (35 N to 40 N) where w is slightly larger (0.02 ms^{-1}) and insoluble aerosol concentration is moderate, $\partial N_i/\partial w$ increases to 0.25 cm^{-3} $m^{-1}s$ due to slightly stronger contributions of homogeneous freezing to N_i. In

the Southern Hemisphere over regions of moderate updraft velocities (0.03 ms^{-1}) such as the South Pacific Gyre, a similar dependence of N_i on w can be seen, although when compared to the Northern Hemisphere sensitivities of N_i to w remain higher (0.1 cm^{-3} $m^{-1}s$). This is because of the lower insoluble aerosol number concentrations here, permitting higher values of f_c and larger contributions of homogeneous freezing to N_i. Over the Antarctic, low insoluble aerosol concentrations and the coldest temperatures globally cause sensitivities of N_i to w to be on the order of 0.25 m^{-3} $m^{-1}s$ which is comparable to regions in the subtropics where updrafts are stronger. Here moderate heterogeneous freezing percentages and cold temperatures increase the potential for additional homogeneous freezing if stronger updrafts were available. Lastly, along the equator where w is strongest and crystal production is dominated by homogeneous freezing, the sensitivity of N_i to w is the highest globally (despite the fact that N_{sulf} is the lowest here), ranging from 0.40 to 0.65 cm^{-3} $m^{-1}s$. Sensitivities here are largely controlled by the strength of w as $\partial N_i/\partial w$ correlates well with w through the previously mentioned power law dependence f_c on w.

3.3.2 Sulfate Number Concentration

N_{sulf} has the strongest influence on N_i when w is large and IN concentrations are low (i.e., when homogeneous freezing is the dominant mode of ice production). This influence is shown in Figure 10b where the global annual average sensitivity of $\partial N_i/\partial N_{sulf}$ is presented. In all regions outside of the tropics, N_i is relatively insensitive to changes in N_{sulf}. In both the Northern Hemisphere and Southern Hemisphere, the small sensitivities are a result of weak updraft velocities (i.e., low values of f_c) and infrequent homogeneous

freezing events (when freezing is purely heterogeneous, $\partial N_i/\partial N_{sulf} = 0.0$). $\partial N_i/\partial N_{sulf}$ is positive in sign globally due to the inability of soluble aerosol to depress supersaturation generation within BN09 and is highest over the tropical oceans where it exceeds 0.016 cm^{-3} cm^3, implying that perturbations in modeled sulfate number concentrations will change N_i by 1.6% of the sulfate number perturbation size. This strong relationship between N_i and N_{sulf} is especially important because of its regional focus in the tropics where radiative fluxes are strongest. Variations in the magnitude of $\partial N_i/\partial N_{sulf}$ can be driven by differences in sulfate number concentration which is seen explicitly after substituting Equation 2 into Equation 3. Here N_i depends on f_c which is scaled by N_{sulf}^{-1}. Because f_c is multiplied by -1 and appears in the exponent of Equation 3, at high enough updraft velocities, N_i in regions limited by N_{sulf} will respond more strongly to changes in N_{sulf} than in regions of high N_{sulf}. This is seen in Figure 10b east of Indonesia along the equator and in the Indian Ocean where region of high updraft are collocated with small sulfate number concentrations. Here $\partial N_i/\partial N_{sulf}$ values are the largest in magnitude globally and can be thought of as a sulfate limited region as adequate cooling is provided by strong updraft velocities, but the lacking presence of sulfate aerosol inhibits ice formation.

3.3.3 Sulfate Geometric Mean Diameter

The global distribution of $\partial N_i/\partial D_{sulf}$ is shown in Figure 10c. Changes to D_{sulf} can impact N_i two ways. First when D_{sulf} is increased, changes to deliquesced droplet volume and hence probability of freezing (since the per volume nucleation rate remains constant) increase, causing increases in f_c. This means increases in D_{sulf} will increase N_i. In addition

to this effect, in BN09, a cutoff diameter for the size of sulfate aerosol allowed to participate in homogeneous freezing is used which is a function of the geometric mean diameter of sulfate. If increases to the geometric mean diameter of the sulfate population are made while the number concentration of sulfate is held constant, the fraction of the population of sulfate that is allowed to freeze can be reduced. Although these two effects influence changes in N_i with opposite signs, the "probability of freezing" impact tends to be much larger than that of the "population size" impact, although the latter becomes increasingly important when homogeneous freezing is infrequent. This can be seen clearly in Figure 10c. $\partial N_i/\partial D_{sulf}$ is positive and largest in magnitude over regions where N_{sulf} is highest, homogeneous freezing is most prevalent, and f_c is large. The sign of $\partial N_i/\partial D_{sulf}$ remains positive but decreases in magnitude at higher latitudes due to smaller f_c values and less homogeneous freezing, implying that in most regions, increases to sulfate size will have a net positive influence on N_i. In the highest latitudes of both the Northern Hemisphere and Southern Hemisphere and over strong dust events, the sign of $\partial N_i/\partial D_{sulf}$ becomes negative as the "population size" effect becomes more important relative to the "probability of freezing" effect due to decreasing contributions of homogeneous freezing to N_i. Overall, increases to D_{sulf} have minimal effects on N_i regardless of region as diameter changes of 1μm would (which would be an increase in the geometric mean diameter of sulfate by a factor of 30), to first order, result in crystal number changes of only 0.025 cm^{-3} ($\partial N_i/\partial D_{sulf}$ = 0.025 $cm^{-3}\mu m^{-1}$ averaged globally).

3.3.4 Temperature

$\partial N_i/\partial T$ is presented in Figure 10d. $\partial N_i/\partial T$ is negative and largest in magnitude where crystal number concentration is high and crystal formation through homogeneous freezing is most prevalent. Here decreases in temperature tend to increase formed crystal number concentration. This effect comes about through the influence of temperature on the per volume homogeneous nucleation rate, which increases with decreasing temperature. The strong correlation of N_i and anti-correlation of heterogeneous freezing percentage with $\partial N_i/\partial T$ suggests that modeled N_i is most sensitive to temperature fluctuations over regions where crystal concentration and homogeneous freezing fraction is largest, where a 1 K decrease in temperature can increase N_i by a maximum of ~4×10^{-3} cm^{-3}. Some regions of positive sensitivities can be observed where heterogeneous freezing is more prevalent meaning here decreases in temperature would decrease N_i. This occurs through modifications to physical properties within BN09, most importantly the diffusivity of water vapor in air. By increasing temperature, the diffusivity of water vapor in air increases meaning water vapor is transported to growing crystals and is depleted at a faster rate during cloud formation, depressing S_{max}, and resulting in lower predicted N_i values. Although this effect persists globally, it is only important over regions of pure heterogeneous freezing such as over Northern Africa where dust events are strongest. Despite all of these effects, when considered globally, the sensitivity of N_i to T is relatively small as large temperature decreases (on the order of 10 K) are required to influence N_i with any significance.

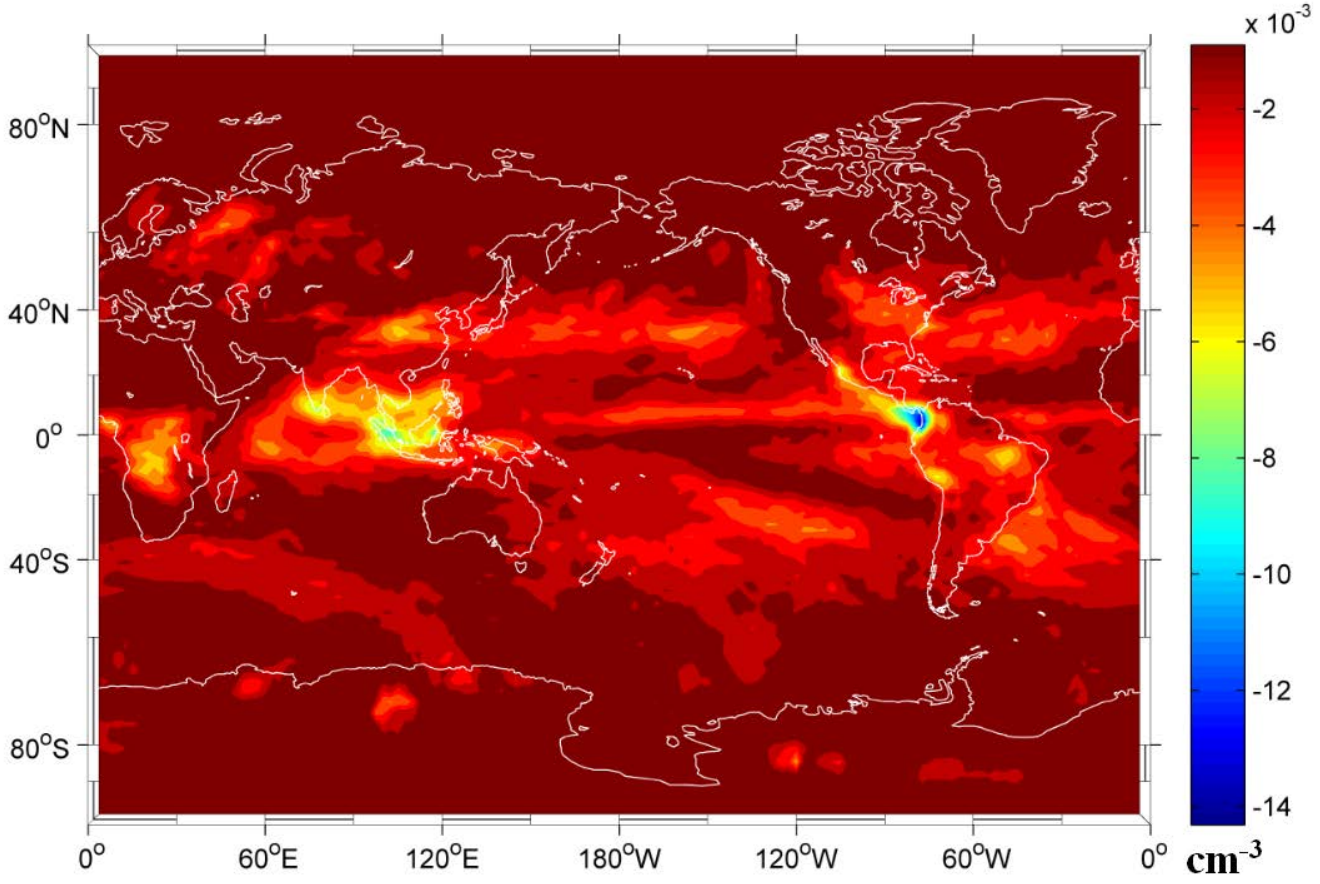

Figure 11: Annually averaged CAM 5.1 cloud formation sensitivity to deposition coefficient (cm^{-3}).

3.3.5 Ice Deposition Coefficient

The global distribution of $\partial N_i/\partial \alpha_d$ is shown in Figure 11. Globally, $\partial N_i/\partial \alpha_d$ is negative and highly correlated with N_i and homogeneous freezing prevalence. By increasing α_d, a larger fraction of the water vapor transported to the surface of growing crystals deposits to the crystal surface, acting to increase the rate at which supersaturation depletion occurs in the forming cloud. Because of this, increases to α_d tend to depress S_{max} in regions of heterogeneous freezing and the strength of homogeneous freezing through decreases to f_c over regions of strong homogeneous freezing. This effect has the largest influence on N_i where the contribution of homogeneous freezing to crystal production is

highest and N_i is largest. The correlation of the strength of homogeneous freezing and α_d suggests that α_d acts on N_i most strongly through its impact on homogeneous crystal production. Averaged globally, the influence of α_d on N_i is relatively weak as a unit change in α_d would decrease N_i by ~3×10^{-3} cm^{-3}. It is important to note that these results are highly dependent on the value of the deposition coefficient chosen (here we use 0.7).

3.3.6 Insoluble Aerosol Number Concentration

Unlike the dependence of N_i on soluble aerosol number concentration, insoluble aerosol number concentration can impact N_i through influences to both $N_{i,het}$ and $N_{i,hom}$. When both heterogeneous and homogeneous freezing are active, adding insoluble aerosol increases N_i through increases in $N_{i,het}$ at the same time, $N_{i,hom}$ is decreased because insoluble aerosol act to reduce f_c. At most cirrus-relevant conditions, the magnitude of the latter is much larger than the former and negative sensitivities result (homogeneous freezing begins to be inhibited by additional insoluble aerosol as seen in Figure 4). The extent to which additional insoluble aerosol inhibit homogeneous freezing is controlled mostly by the magnitude of w; when updraft velocities are strong, decreases in f_c are buffered from the larger water vapor sink of more IN, resulting in small, negative sensitivities to insoluble aerosol number. At weaker updrafts, the reduction in $N_{i,hom}$ from adding insoluble aerosol becomes larger as greater marginal reductions in f_c occur (Figure 4). When in this regime of BN09, the sensitivity of N_i to insoluble aerosol is large in magnitude and negative. If insoluble aerosol concentrations are large enough, homogeneous freezing can be completely inhibited and additional insoluble aerosol will act to only increase N_i, making the sensitivity of N_i to insoluble aerosol number

concentration positive although relatively small in magnitude [35]. The global occurrence and distribution of these dependencies for insoluble dust, black carbon, and organic carbon number concentration within CAM 5.1 is presented in Figure 12 and discussed below.

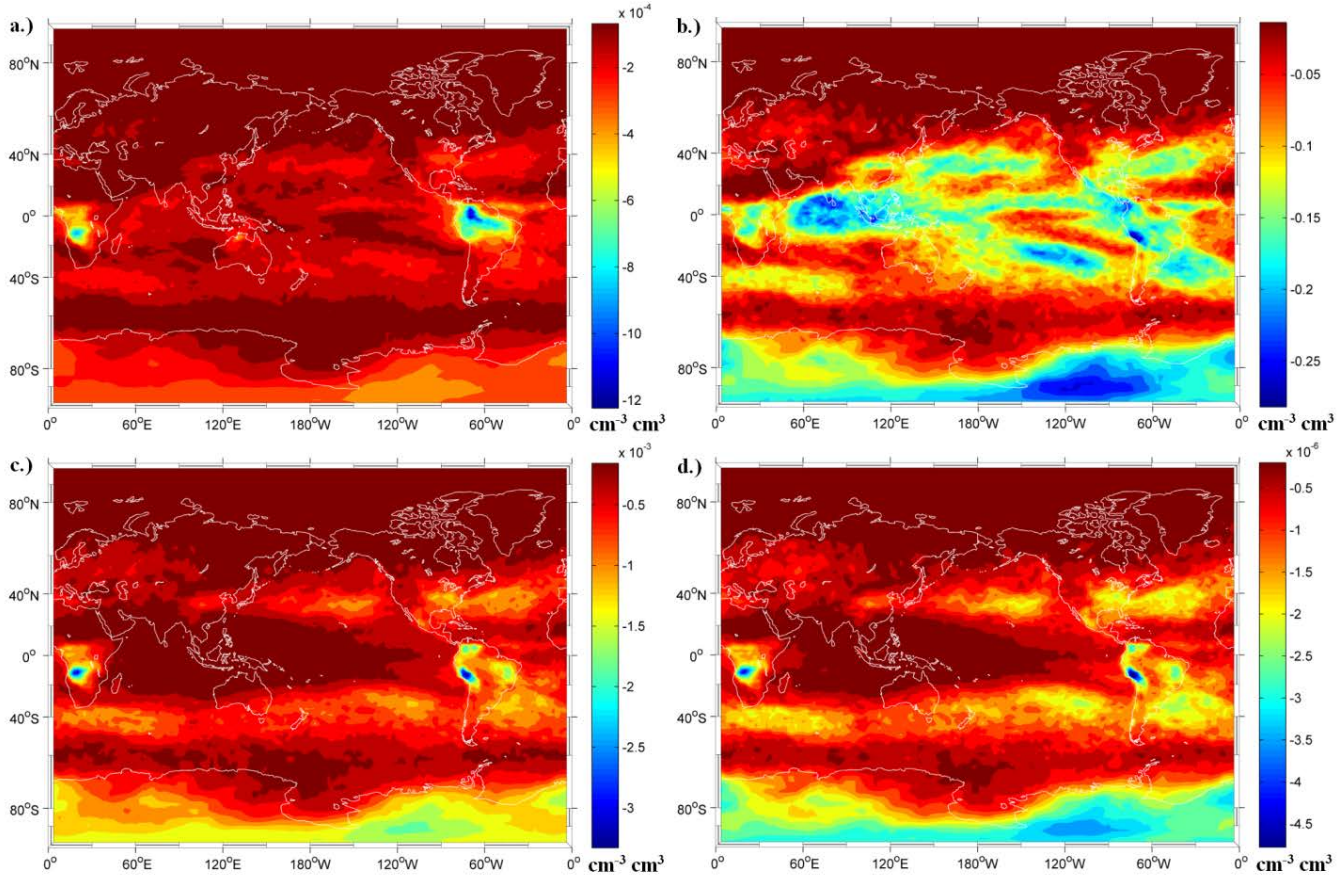

Figure 12: Annually averaged CAM 5.1 cloud formation sensitivities to insoluble aerosol number concentration; a.) Accumulation mode dust (cm^{-3} cm^{3}), b.) Coarse mode dust (cm^{-3} cm^{3}), c.) Black carbon (cm^{-3} cm^{3}), d.) Organic carbon (cm^{-3} cm^{3}).

Over the tropics where crystal production originates mostly from homogeneous freezing, strong updrafts and relatively low background insoluble aerosol concentrations allow S_{max} to frequently reach S_{hom}. Here increases in insoluble aerosol concentration act to shut down homogeneous freezing (although weakly due to the strength of w) through

slight changes to f_c. This can be seen in all subplots of Figure 12 where the sensitivity of N_i to insoluble aerosol concentration is relatively weak and negative for all insoluble aerosol species. In these regions, sensitivities to insoluble aerosol number range from -0.2 to -0.5 × 10^{-6} cm^{-3} cm^3. The relative magnitude of each of the sensitivity fields is a reflection of how efficiently each species can act as an IN through the amount of water vapor they deplete during cloud formation. Coarse mode dust and black carbon number concentration have the strongest impact on N_i where its efficient ice nucleating characteristics and moderate concentrations result in sensitivities equal to -0.2 $cm^{-3}cm^3$ to -0.5×10^{-3} $cm^{-3}cm^3$ respectively. The distribution of sensitivities of N_i to coarse mode dust are distributed somewhat differently than the other three insoluble aerosol species; $\partial N_i/\partial N_{dust,c}$ is negative and largest in magnitude whereas the sensitivities for other insoluble aerosol species tend to be weaker. This suggests that despite the presence of strong updrafts and low heterogeneous freezing percentages, additional coarse mode dust can strongly reduce f_c (the model state shifts to the regime of combined homogeneous/heterogeneous freezing where insoluble aerosol strongly decrease N_i associated with the steep downward section of the curve in Figure 4). This means that over these regions N_i is strongly influenced by variations in only coarse mode dust (a single additional coarse mode dust aerosol will decrease N_i by up to ~0.20 cm^{-3}) because N_i is strongly buffered from the influence of other insoluble aerosol due to large w. This influence from coarse mode dust is a result of the high surface area and efficient ice nucleating ability of this type of insoluble aerosol when compared to the other insoluble aerosol species.

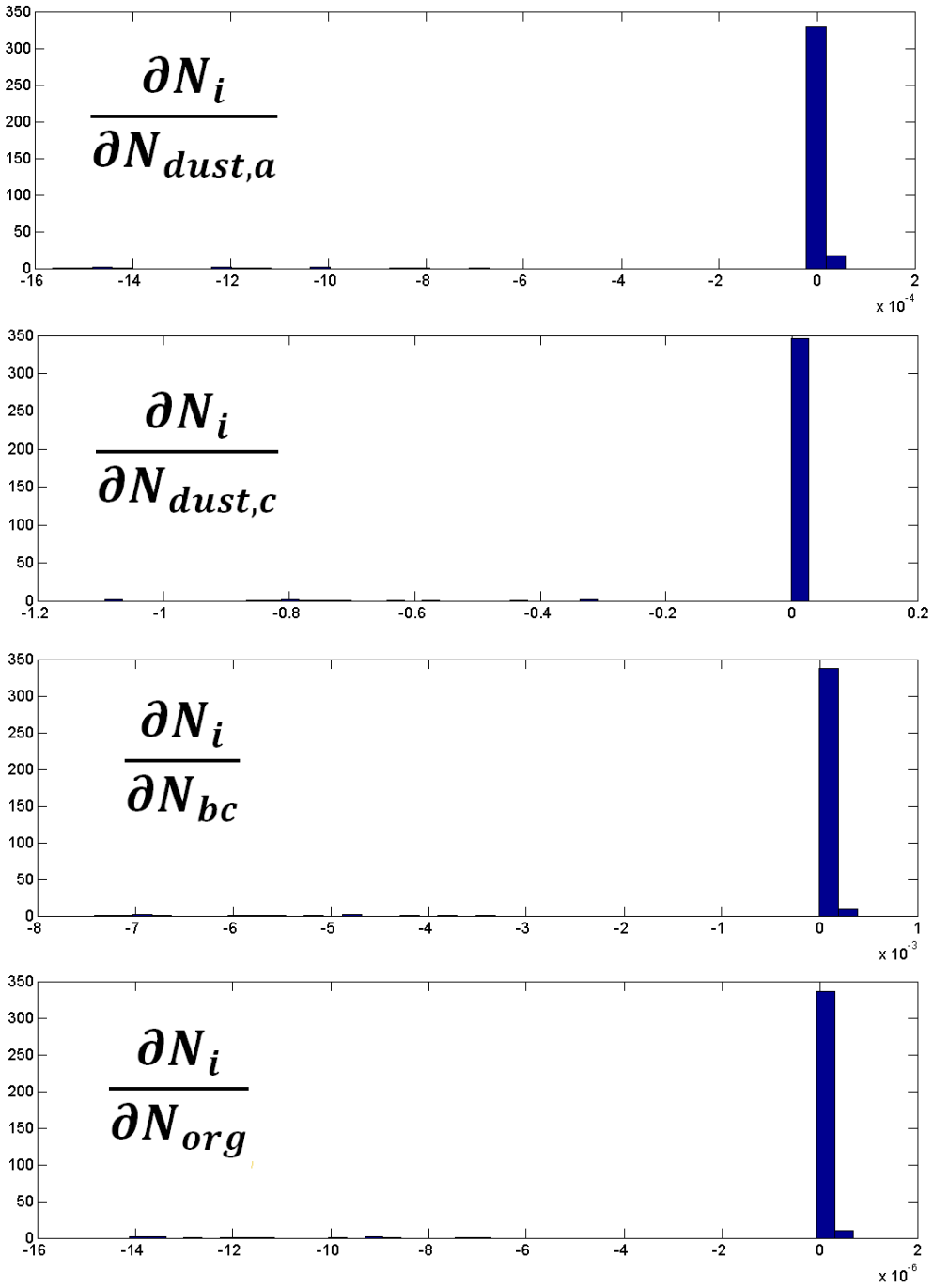

Figure 13: Distributions of insoluble aerosol number concentration sensitivities from regions where sensitivities are small in magnitude and negative when annually averaged; Sensitivities are on the horizontal axis (cm^{-3} cm^{-3}) and frequency of occurrence on the vertical axis.

In the high latitudes of the Northern Hemisphere, crystal production is dominated by heterogeneous freezing due to weak updraft velocities and relatively high background insoluble aerosol number concentrations. Because of how N_i is influence by insoluble aerosol number in BN09, one would expect sensitivities to insoluble aerosol number to be positive here (crystal production is almost purely heterogeneous), however annually averaged sensitivities are negative and small in magnitude (equal to ~ -1.0×10^{-4} cm^{-3} cm^{3}). The root of this inconsistency can be explained by examining the annual distribution of sensitivities of N_i to insoluble aerosol number concentration from a single grid box in the Northern Hemisphere, which is presented in Figure 13. For all insoluble aerosol species, sensitivities are positive and relatively weak in magnitude for more than 92% of the time steps of the year-long integration.

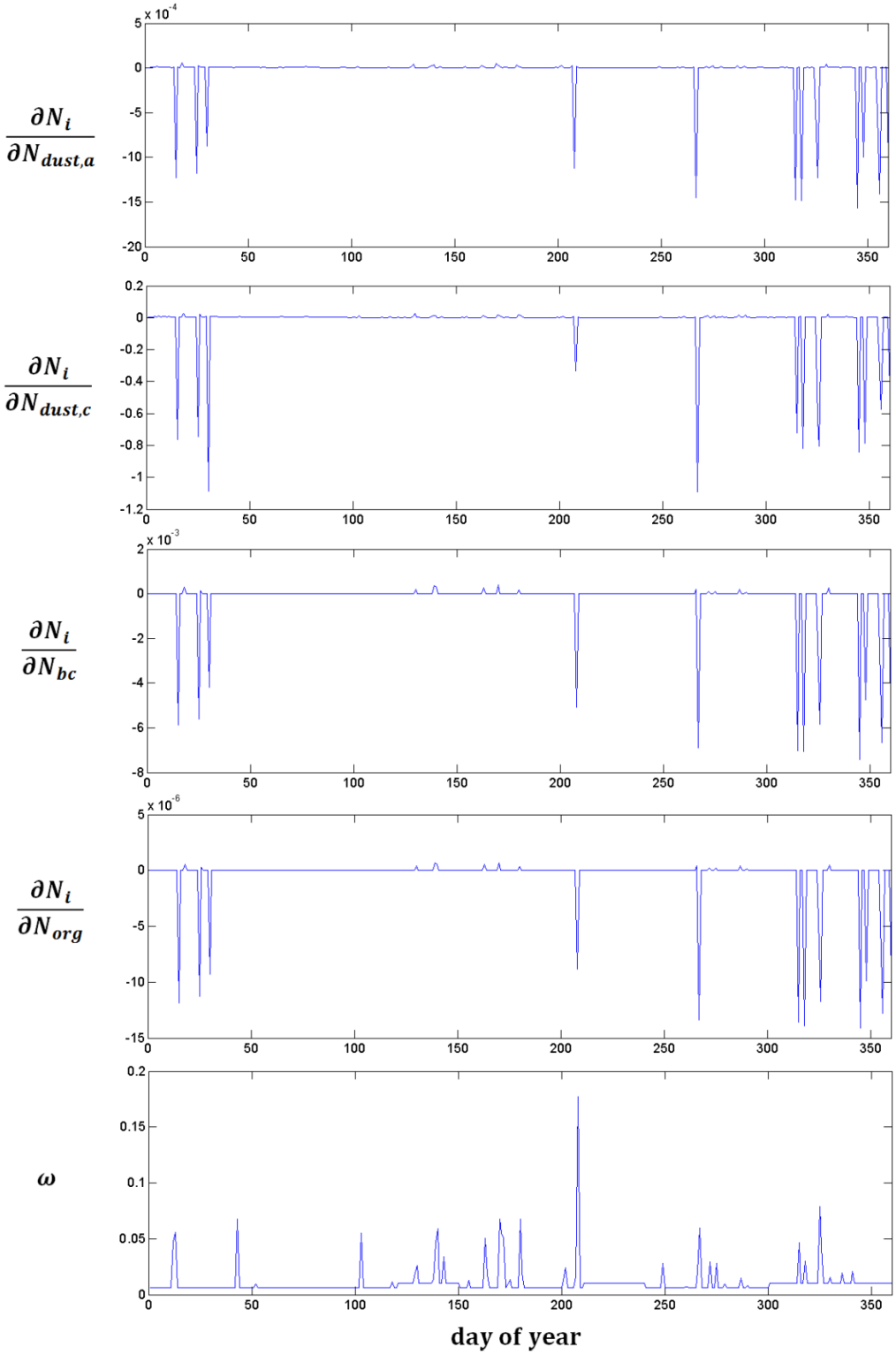

Figure 14: Time series of insoluble aerosol number concentration sensitivities and updraft velocity from regions where sensitivities are small in magnitude and negative when annually averaged; Sensitivities are presented in (cm^{-3} cm^{-3}) and updraft velocity in (ms^{-1}).

The remaining days of the year consist of large, negative sensitivities, characteristic of strong competition between homogeneous and heterogeneous freezing. Figure 14 shows the time series of the sensitivity of N_i to insoluble aerosol number and w from the same grid box as presented in Figure 13. For all insoluble aerosol species, the anomalous events of strongly negative sensitivities are located in time with the peaks of strong updrafts. When considered annually, these extreme events shift the sensitivity of N_i to insoluble aerosol number concentration to large, negative values for all aerosol species, despite this region being dominated by heterogeneous crystal production.

In the Southern Hemisphere, N_i is also controlled by heterogeneous freezing. Here the previously mentioned influence of sporadic, extreme updraft events on sensitivities of N_i to insoluble aerosol number is even stronger as sensitivities are negative and larger in magnitude when compared to the Northern Hemisphere. This is because in the Southern Hemisphere, updraft velocities are of similar magnitude to the Northern Hemisphere, but insoluble aerosol number concentrations are lower. Because of this, heterogeneous freezing still dominates crystal production, but BN09 lies at a model state closer to the transition to pure heterogeneous freezing when compared to the Northern Hemisphere (the number of insoluble aerosol found in the Southern Hemisphere is only slightly larger than N_{lim}). Because of this, small, positive variations in w can cause significant chances in which freezing regimes control ice formation. Here significant reductions in $N_{i,hom}$ through large reductions in f_c occur when the number concentration of insoluble aerosol is increased; when compared to the Northern Hemisphere, these shifts tend to happen more easily and influence N_i to a larger extent. For example in the Southern Hemisphere, adding 1.0 cm^{-3} of accumulation mode dust aerosol can decrease N_i by as much as

2.0×10^{-4} cm^{-3}, whereas this result is lower by a factor of two in the Northern Hemisphere. It is important to also mention the role temperature plays in establishing sensitivities scales over the Antarctic. In PDA 2008, decreases in temperature cause increases in the ice nucleating ability of insoluble aerosol through changes to μ_i. Because of this, and the frequent shift in freezing regimes, sensitivities to insoluble aerosol number concentration are largest in magnitude over the coldest regions of the Southern Hemisphere and are likely to become stronger at higher altitudes where insoluble aerosol number concentration is lower and temperatures are colder.

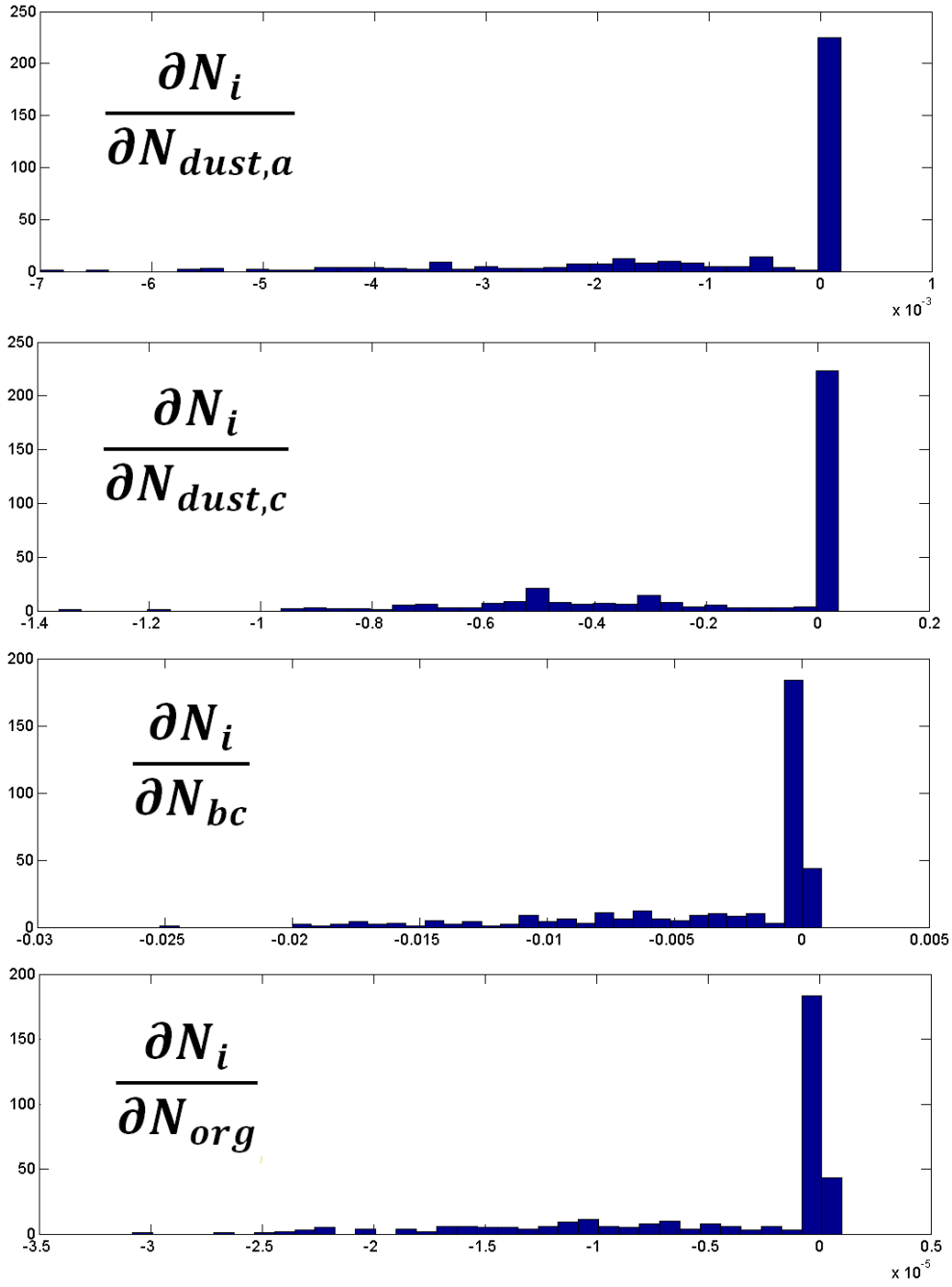

Figure 15: Distributions of insoluble aerosol number concentration sensitivities from regions where sensitivities are large in magnitude and negative when annually averaged; Sensitivities are on the horizontal axis (cm^{-3} cm^{-3}) and frequency of occurrence on the vertical axis.

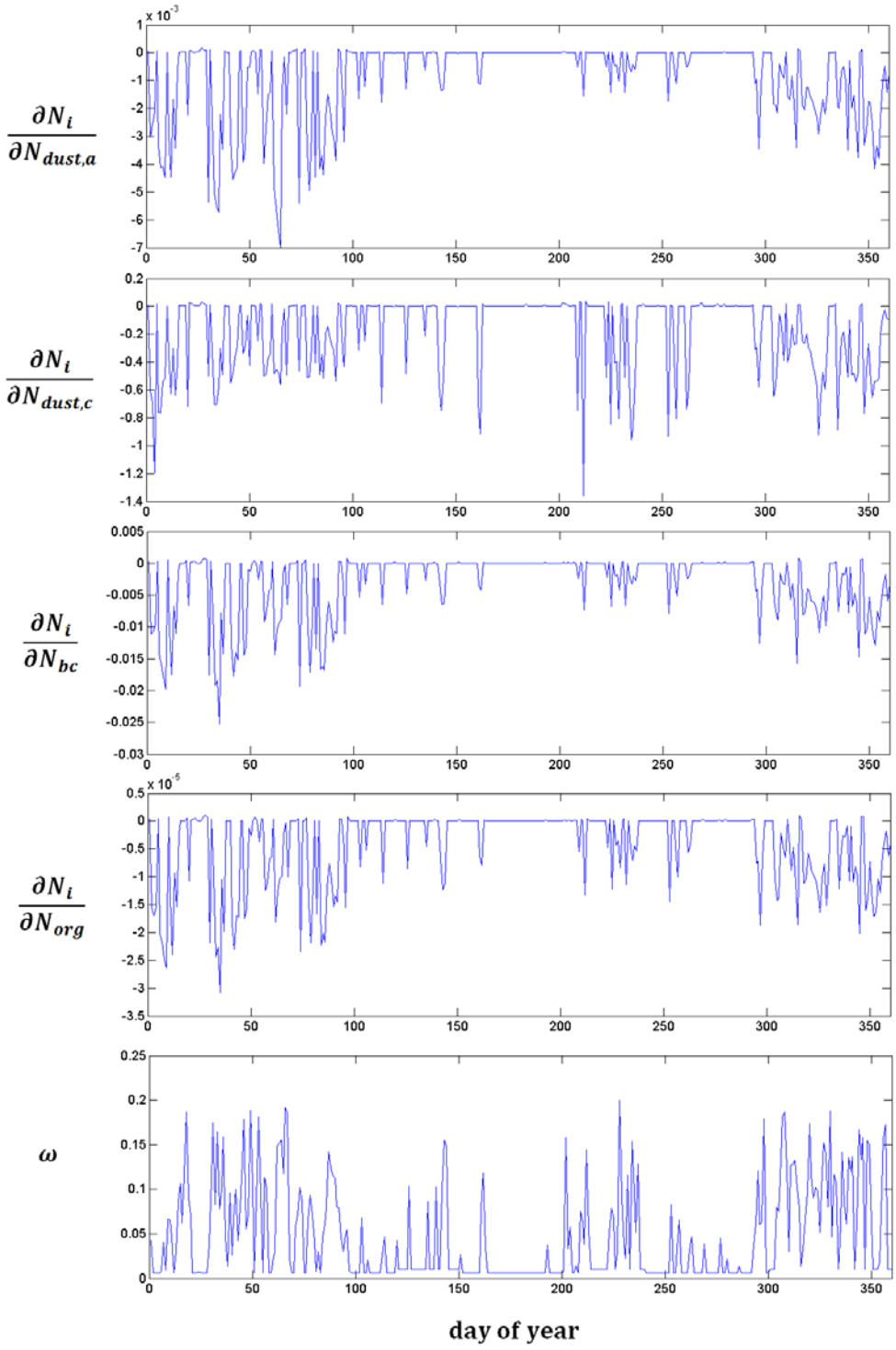

Figure 16: Time series of insoluble aerosol number concentration sensitivities and updraft velocity from regions where sensitivities are large in magnitude and negative when annually averaged; Sensitivities are presented in (cm^{-3} cm^{-3}) and updraft velocity in (ms^{-1}).

Although crystal production is dominated by heterogeneous freezing globally, the model state of BN09 within CAM 5.1 frequently lies close to the point of transition between pure heterogeneous freezing and homogeneous and heterogeneous freezing. For all aerosol species, this effect has the strongest influence on annually averaged sensitivities of N_i to insoluble aerosol number over a highly localized region of Central Africa and South America (dark blue bullseyes in Figure 12). The frequency distributions and time series of updraft and sensitivities to insoluble aerosol number concentration over Central Africa are presented in Figure 15 and Figure 16 respectively. It can be seen that more (although still relatively infrequent) model realizations at states where homogeneous freezing is strongly inhibited occur than in the rest of the globe. Like before, these events correlate in time with anomalously large *w* events as seen in Figure 16. Additionally, an annual cycle in *w* and sensitivities to insoluble aerosol number for all aerosol species exists, illustrating that although these shifts between freezing regimes occurs sporadically due to fluctuations in the turbulence simulated in CAM 5.1, they tend to be driven by large scale climatic features such as the annual cycle of solar radiative fluxes. The large effect that a few, highly negative sensitivities can have on the annually averaged sensitivities of N_i to insoluble aerosol number concentration is an important point to consider when computing the climatic susceptibility of regions to changes in insoluble aerosol concentrations. It can be seen that small shifts in updraft velocity computed in within CAM 5.1 can cause significant shifts in the freezing regimes responsible for crystal formation and the magnitude of N_i. This implies that special care should be taken in the computation of *w* from TKE in CAM 5.1. The large magnitude of these anomalous events suggests that when considering the regional influence of

insoluble aerosol number concentration on N_i, daily variations in dynamic fields can skew the annually averaged sensitivity of N_i and may not be important to consider when characterizing the susceptibility of a region to perturbations in model state on longer time scales.

3.3.7 Insoluble Aerosol Geometric Mean Diameter

As was seen with insoluble aerosol number concentration, N_i is impacted by changes to insoluble aerosol geometric mean diameter through effects on both $N_{i,het}$ and $N_{i,hom}$; these influences come about through changes to the fraction of insoluble aerosol that freeze at a given supersaturation and by affecting the fraction of the soluble aerosol population that freeze respectively.

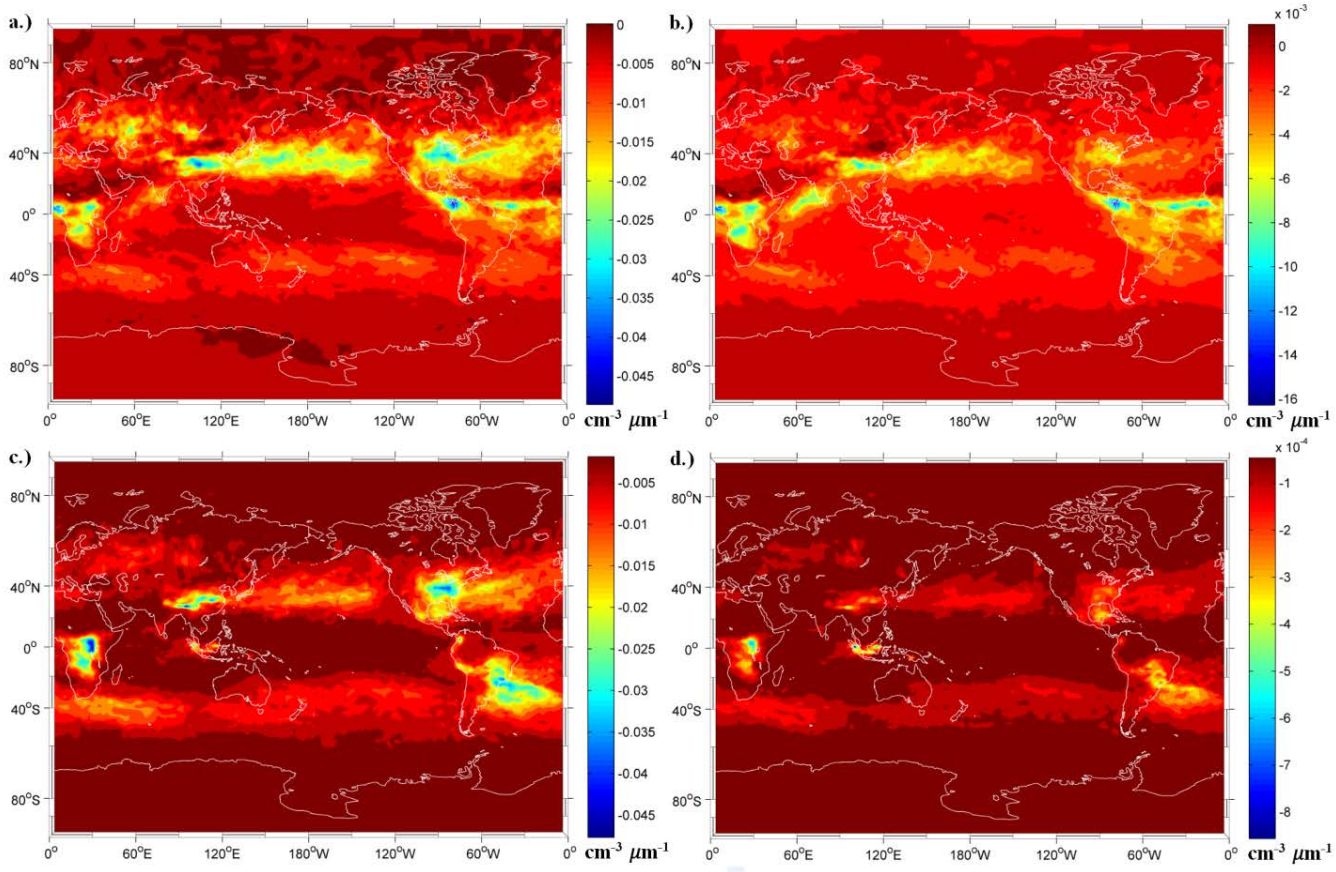

Figure 17: Annually averaged CAM 5.1 cloud formation sensitivities to insoluble aerosol geometric mean diameter; a.) Accumulation mode dust ($cm^{-3}\ \mu m^{-1}$), b.) Coarse mode dust ($cm^{-3}\ \mu m^{-1}$), c.) Black carbon ($cm^{-3}\ \mu m^{-1}$), d.) Organic carbon ($cm^{-3}\ \mu m^{-1}$).

Following PDA 2008, the geometric mean diameter of each insoluble aerosol species is used to define $dN_{IN,i}/dlogD_i$ in Equation 5. Increasing the geometric mean diameter of a given distribution of insoluble aerosol changes the shape of $dN_{IN,i}/dlogD_i$ by increasing the number concentration of aerosol at larger diameters. Because the active site density remains constant for all aerosol species this shift in the number of aerosol to larger diameters will result in more insoluble aerosol with large numbers of active sites (low values μ_i). In other words, the fraction of aerosol that will freeze at a given size, as defined by μ_i, will be large at sizes where now higher number concentrations of insoluble aerosol exist. Because of this, increases to the geometric mean diameter of all insoluble

aerosol species will increase $N_{i,het}$ at a given supersaturation. In BN09, when homogeneous freezing and heterogeneous freezing are both active, increases to $N_{i,het}$ tends to reduce N_i as less of the soluble aerosol population freezes homogeneously when compared to the increases in $N_{i,het}$. If freezing is purely heterogeneous, increases to $N_{i,het}$ only increase N_i, although to a small extent. The global distributions of the sensitivity of N_i to insoluble aerosol geometric mean diameter for all insoluble aerosol species is shown in Figure 17, where three distinct regimes can be observed.

The first regime, which is defined by regions of low heterogeneous freezing percentage, is concentrated over the tropical Pacific Ocean. The sensitivity of N_i to insoluble aerosol geometric mean diameter is smallest in magnitude here and slightly negative owing to weak inhibitions of homogeneous freezing. This inhibition is a result of strong updraft cooling, which acts to buffer f_c from increased $N_{i,het}$ due to changes in the geometric mean diameter of insoluble aerosol. Sensitivities range from -9.0×10^{-4} cm^{-3} μm^{-1} for organic carbon to -5.0×10^{-3} cm^{-3} μm^{-1} for black carbon. Again, the relative magnitudes of sensitivities across aerosol is a metric of how efficiently each species of insoluble aerosol can serve as IN and deplete supersaturation generation during cloud formation. The species of insoluble aerosol that responds strongest to changes in geometric mean diameter is black carbon, where to first order a 1 μm change in geometric mean diameter will decrease N_i by 5.0×10^{-3} cm^{-3}. This shows that despite the strong ice nucleating ability of black carbon, N_i responds relatively weakly to even unrealistically large perturbations in aerosol size characteristics.

The second regime of insoluble aerosol diameter influence on N_i can be found outside of the tropics in the Southern Hemisphere, where freezing is almost purely

heterogeneous and sensitivities of N_i to insoluble aerosol geometric mean diameter are negative and greater in magnitude than in the tropics for all aerosol species. Because crystal production is dominated by heterogeneous freezing, it is expected that sensitivities to insoluble geometric mean diameter would be positive as increases to insoluble aerosol size increases $N_{i,het}$. As was the case with insoluble aerosol number, this discrepancy is a result of infrequent model realizations at states where homogeneous freezing starts to become inhibited. These realizations contribute large, negative sensitivities to the annual average sensitivity fields, resulting in net positive sensitivities to geometric mean diameter. As was seen for insoluble aerosol number, this effect becomes stronger as w becomes larger because shifts to combined homogeneous and heterogeneous freezing occur more frequently. This is illustrated in Figure 17, where sensitivities of N_i to insoluble aerosol geometric mean diameter decrease in magnitude by a factor of three when moving from 40 S (where w = 0.02 ms^{-1}) to 80 S (where w = 0.001 ms^{-1}). When establishing model dependencies to insoluble aerosol size information over regions like these, special consideration of the influence of these extreme events can have should be made as shifts between freezing regimes are common and can greatly skew sensitivity information.

The last of the three regimes can be found in the mid-latitudes of the Northern Hemisphere where accumulation and coarse mode dust number concentration are highest (i.e., over North Africa and the Pacific Ocean at 40 N). In this region, heterogeneous freezing percentage is the highest globally due to the largest accumulation and coarse mode dust number concentrations. Annually averaged sensitivities of N_i to both accumulation and coarse mode dust are positive and low small in magnitude meaning the

previously mentioned effect of extreme updraft events on the sign of annually averaged sensitivities (discussed above in the second regime) is unimportant. This occurs because background dust concentrations are so high that even large, positive fluctuations in w cannot shift BN09 from pure heterogeneous freezing to combined homogeneous and heterogeneous freezing. The positive sensitivities in this region are small in magnitude ($\partial N_i/\partial D_{dust,a}$ = 0.5×10^{-5} cm^{-3} μm^{-1} , $\partial N_i/\partial D_{dust,c}$ = 0.5×10^{-4} cm^{-3} μm^{-1}), illustrating the weak response changes in insoluble aerosol size have on N_i over regions of even pure heterogeneous crystal production. Globally, even large changes to insoluble aerosol diameter (on the order of 1 μm) have minor impacts on N_i (sensitivities to insoluble diameter are at most -0.048 $cm^{-3}\mu m^{-1}$).

CHAPTER 4

USING ICE CRYSTAL SENSITIVITY INFORMATION TO QUANTIFY SOURCES OF ICE CRYSTAL NUMBER VARIABILITY IN CAM 5.1

4.1 Motivation

Often in global model simulations, the extent to which variability in model inputs drives variability in microphysical cloud properties can be challenging to assess; this is especially true for properties related to cloud formation which can be highly non-linear functions of model inputs. To address this issue, we use the sensitivity information computed from ABN09 to quantify the extent to which varying input fields drive variability in N_i within CAM 5.1.

4.2 Description of First Order Variability Attribution Calculations

We achieve this by considering both the sensitivity of N_i to each varying parameterization input as well as the magnitude of variability for each parameterization inputs throughout the CAM 5.1 integration. The variability of parameterization inputs fields in each global model grid box is represented by the local standard deviation of that field computed with daily temporal resolution for the annual global model simulation, σx_j, where x_j is any of the varying input fields to BN09 (the fields are presented in the first column of Table 3).

Table 3: Contributions to variability in crystal number concentration in CAM 5.1

x_j	Mean Global $\xi N_i x_j$ (%)	STD Global $\xi N_i x_j$ (%)	Mean Global $\partial N_i/\partial x_j\|_n / \sigma x_j\|_n$	STD Global $\partial N_i/\partial x_j\|_n / \sigma x_j\|_n$
w	38.20	19.26	1.11	4.28
N_{sulf}	23.25	28.34	1.42	3.98
D_{sulf}	0.983	0.7632	1.05	0.61
T	15.71	11.61	1.51×10^{3}	9.00×10^{2}
$N_{dust,a}$	5.012	6.182	0.23	0.40
$D_{dust,a}$	0.577	0.510	5.18	7.66
$N_{dust,c}$	11.73	11.80	0.13	0.20
$D_{dust,c}$	0.952	0.882	4.00	4.07
N_{bc}	3.121	5.680	0.17	0.38
D_{bc}	0.411	0.413	3.18	4.05
N_{org}	0.052	0.101	2.30×10^{-3}	6.30×10^{-3}
D_{org}	0.004	0.004	0.03	0.05

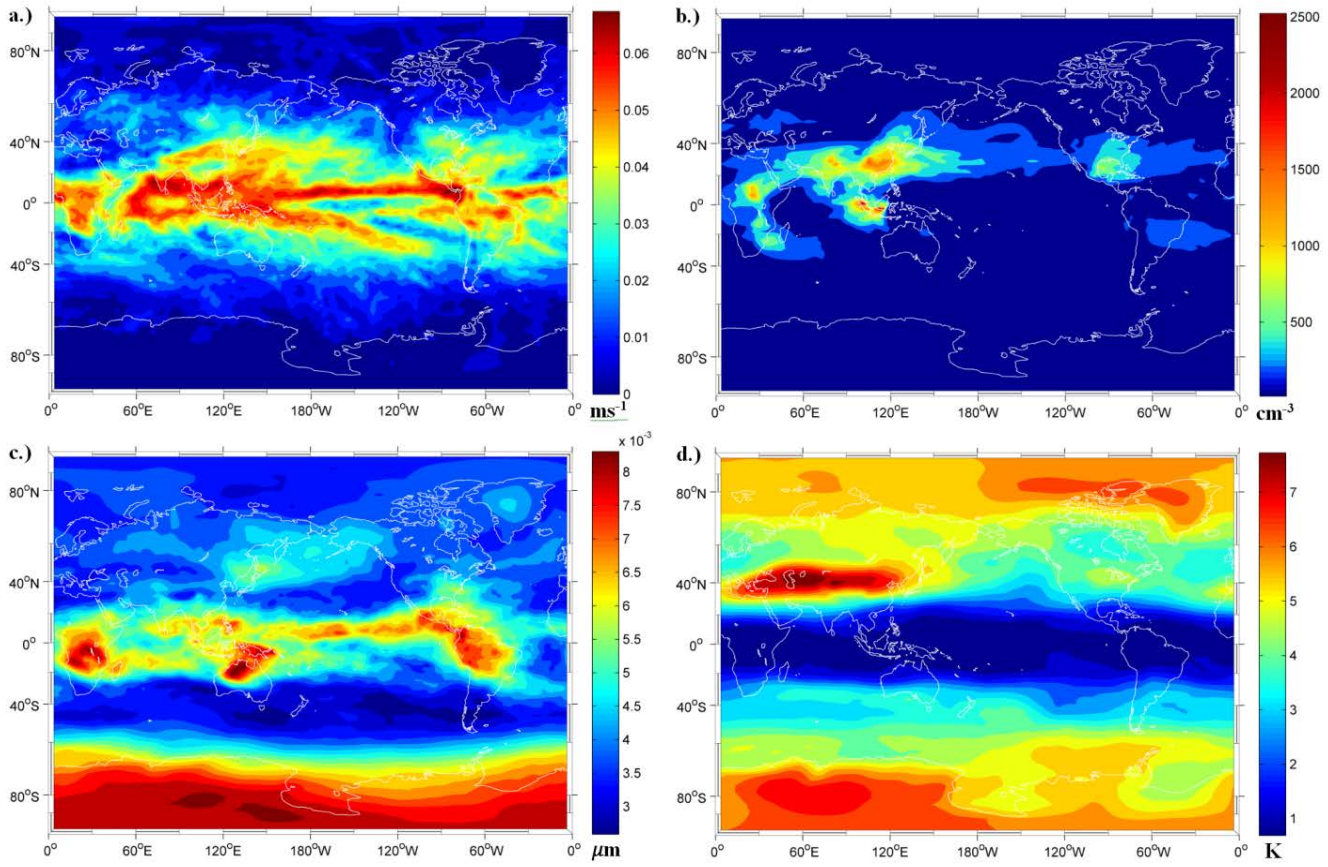

Figure 18: Global distributions of the daily standard deviation of; a.) Updraft velocity (ms^{-1}), b.) Sulfate number concentration (cm^{-3}), c.) Sulfate geometric mean diameter (μm), d.) Temperature (K).

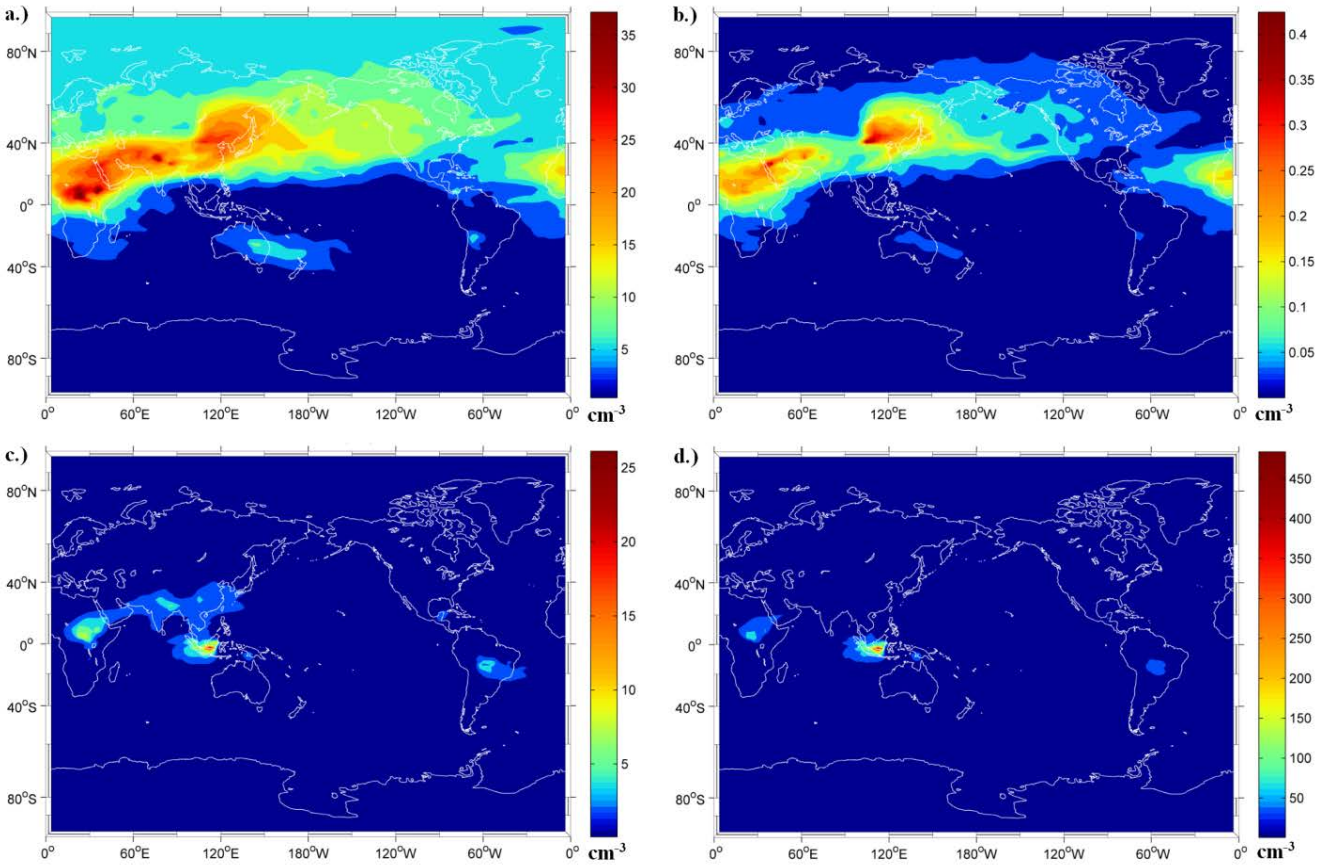

Figure 19: Global distributions of the daily standard deviation of; a.) Accumulation mode dust number concentration (cm^{-3}), b.) Coarse mode dust number concentration (cm^{-3}), c.) Black carbon number concentration (cm^{-3}), d.) Organic carbon number concentration (cm^{-3}).

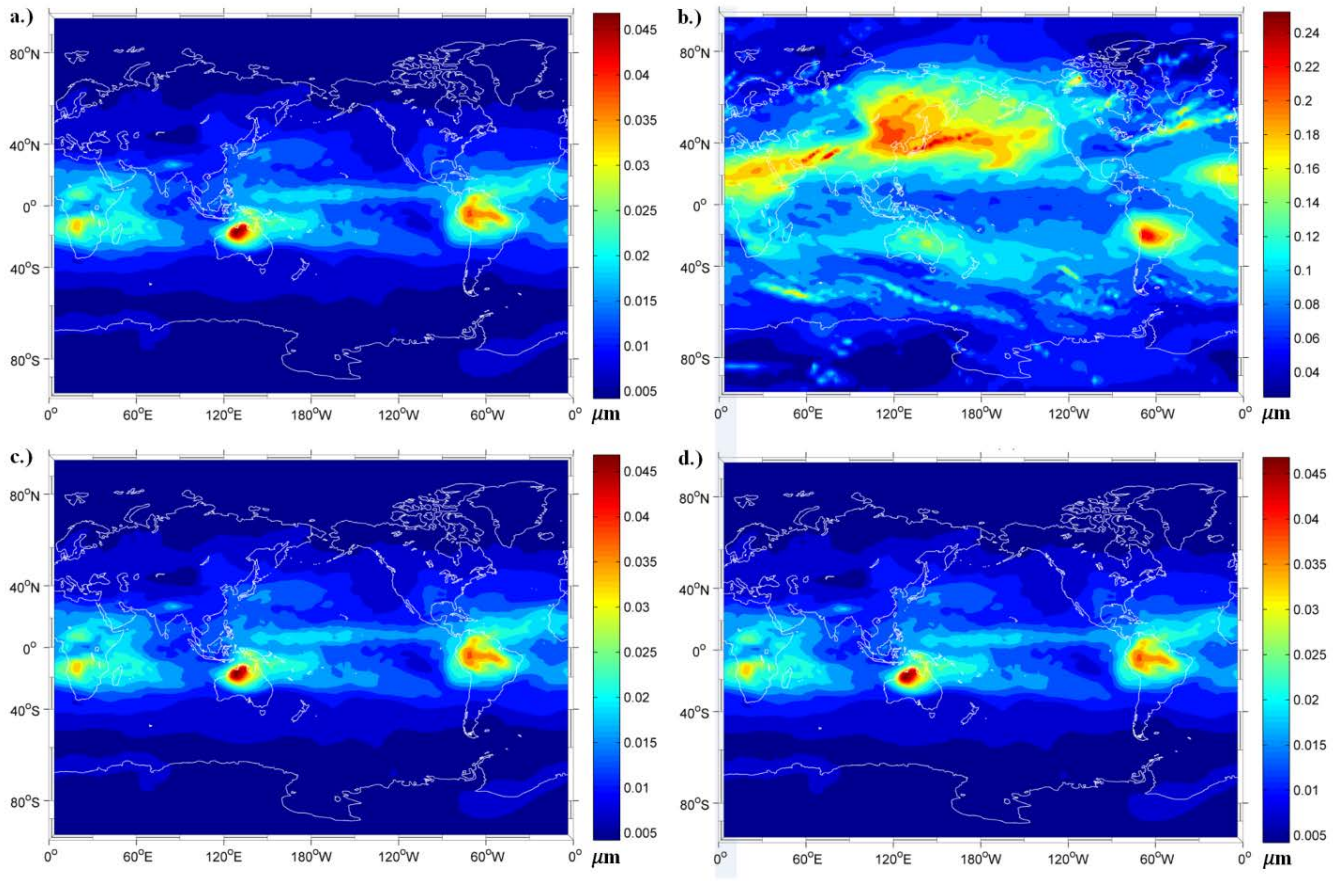

Figure 20: Global distributions of the daily standard deviation of; a.) Accumulation mode dust geometric mean diameter (μm), b.) Coarse mode dust geometric mean diameter (μm), c.) Black carbon geometric mean diameter (μm), d.) Organic carbon geometric mean diameter (μm).

We choose to compute daily standard deviations for each variable as one day is the characteristic timescale of stratiform ice cloud formation and persistence; the global distributions of standard deviations are presented in Figure 18, Figure 19, and Figure 20 for all fields found in the first column of Table 3. The magnitude of the sensitivity of N_i to x_j within each grid box is defined as the absolute value of the annually averaged sensitivities computed from ABN09, $|\partial N_i/\partial x_j|$. Ignoring higher order and cross derivative terms, the contribution of field x_j to N_i variability, $\sigma N_{i,j}$, can be written as the product of $|\partial N_i/\partial x_j|$ and σx_j (Equation 7).

$$\sigma N_{i,j} = \left|\frac{\partial N_i}{\partial x_j}\right| \sigma x_j \qquad (7)$$

The contribution of all input fields to the total variability in N_i, σN_i, can then be written by summing Equation 7 over j for all input fields, x_j (Equation 8),

$$\sigma N_i = \sum_j \left|\frac{\partial N_i}{\partial x_j}\right| \sigma x_j \qquad (8)$$

The relative contribution of a given input parameter, x_j, to modeled variability of N_i is then obtained by dividing Equation 7 for a given j by Equation 8, defined as $\xi N_i x_j$. This calculation was performed at all grid points for all fields and is presented in Table 3 along with global statistics of $\xi N_i x_j$ and a comparison of the relative importance of model sensitivity and variability scales for each model field. The relative importance of model sensitivity and model input variability for each input field are assessed by computing the ratio of the fully normalized sensitivity and the fully normalized standard deviation in each grid box. Fully normalized sensitivities, $\left.\frac{\partial N_i}{\partial x_j}\right|_n$, are defined as the absolute value of the local annual average sensitivity multiplied by the ratio of the local annual average crystal number concentration, $\overline{N_i}$, to the annual average value of the input variable, $\overline{x}_j$ (Equation 9),

$$\left.\frac{\partial N_i}{\partial x_j}\right|_n = \frac{\overline{x_j}}{\overline{N_i}} \left|\frac{\partial N_i}{\partial x_j}\right| \qquad (9)$$

Fully normalized standard deviations for each field, $\sigma x_j\big|_n$, are defined as σx_j divided by the annual average value of the input variable, $\overline{x}_j$ (Equation 10),

$$\sigma x_j\big|_n = \frac{\sigma x_j}{\overline{x_j}} \qquad (10)$$

For a given field, the ratio of normalized sensitivity to normalized variability quantifies which of the two terms (inherent model sensitivity or variability in model inputs) contributes more to $\xi N_i x_j$. When larger than unity, $\xi N_i x_j$ is driven more by inherent model sensitivity than input field variability for a given x_j and when less than unity, the opposite holds. For ratios on the order of unity, both the model sensitivity to inputs and modeled variability of input fields are of similar importance to $\xi N_i x_j$.

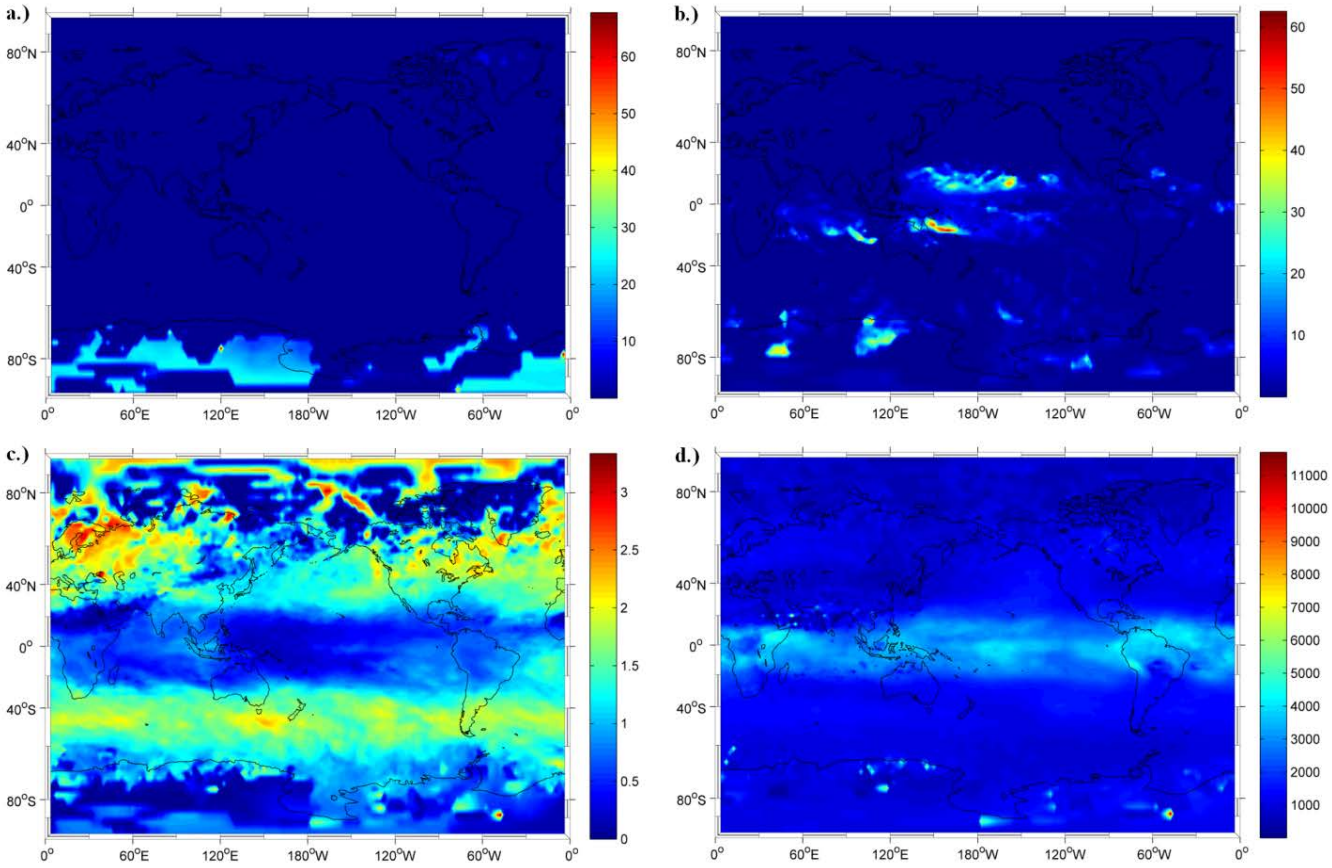

Figure 21: Annually averaged distributions of the ratio of normalized sensitivity to normalized standard deviation of; a.) Updraft velocity, b.) Sulfate number concentration, c.) Sulfate geometric mean diameter, d.) Temperature.

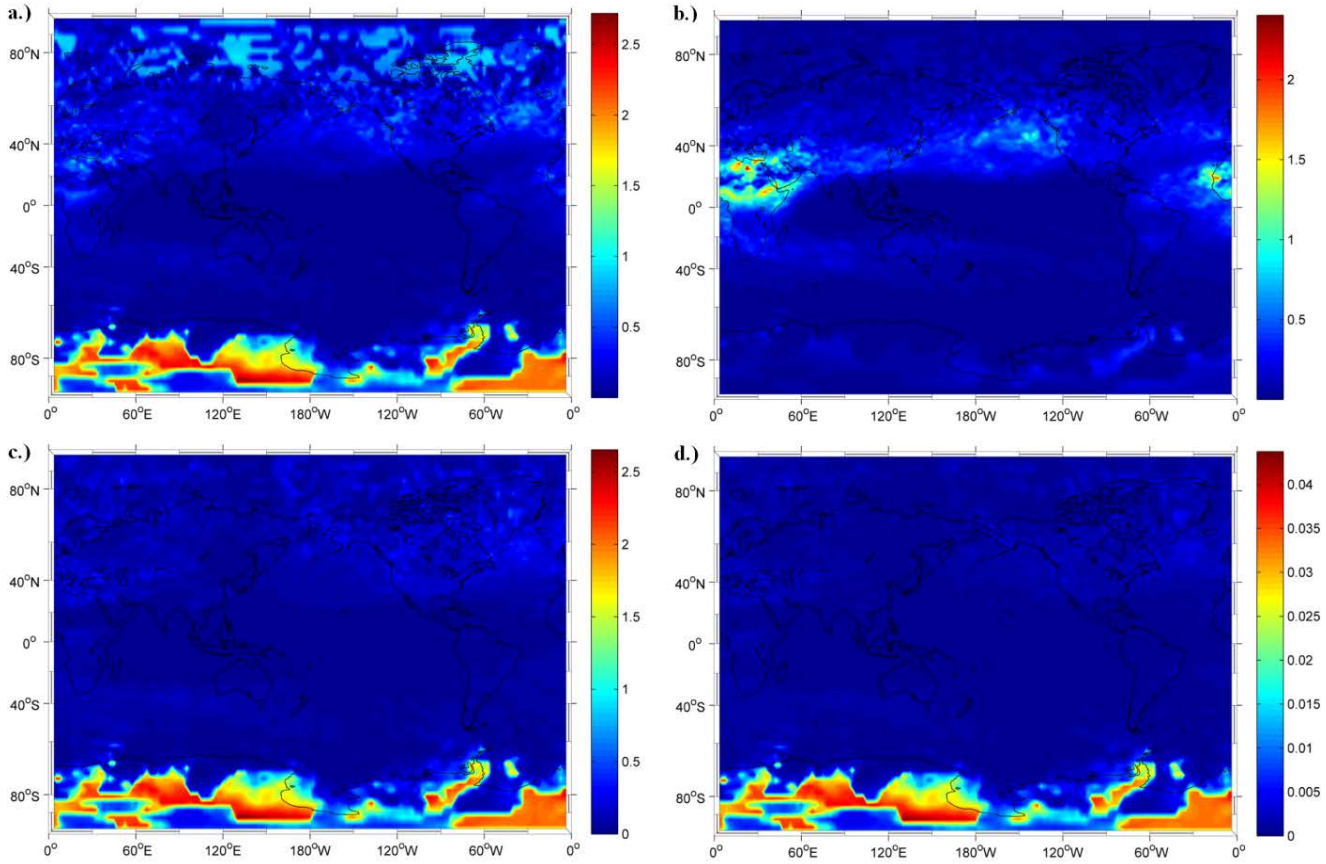

Figure 22: Annually averaged distributions of the ratio of fully normalized sensitivities to normalized standard deviations of; a.) Accumulation mode dust number concentration, b.) Coarse mode dust number concentration, c.) Black carbon number concentration, d.) Organic carbon number concentration

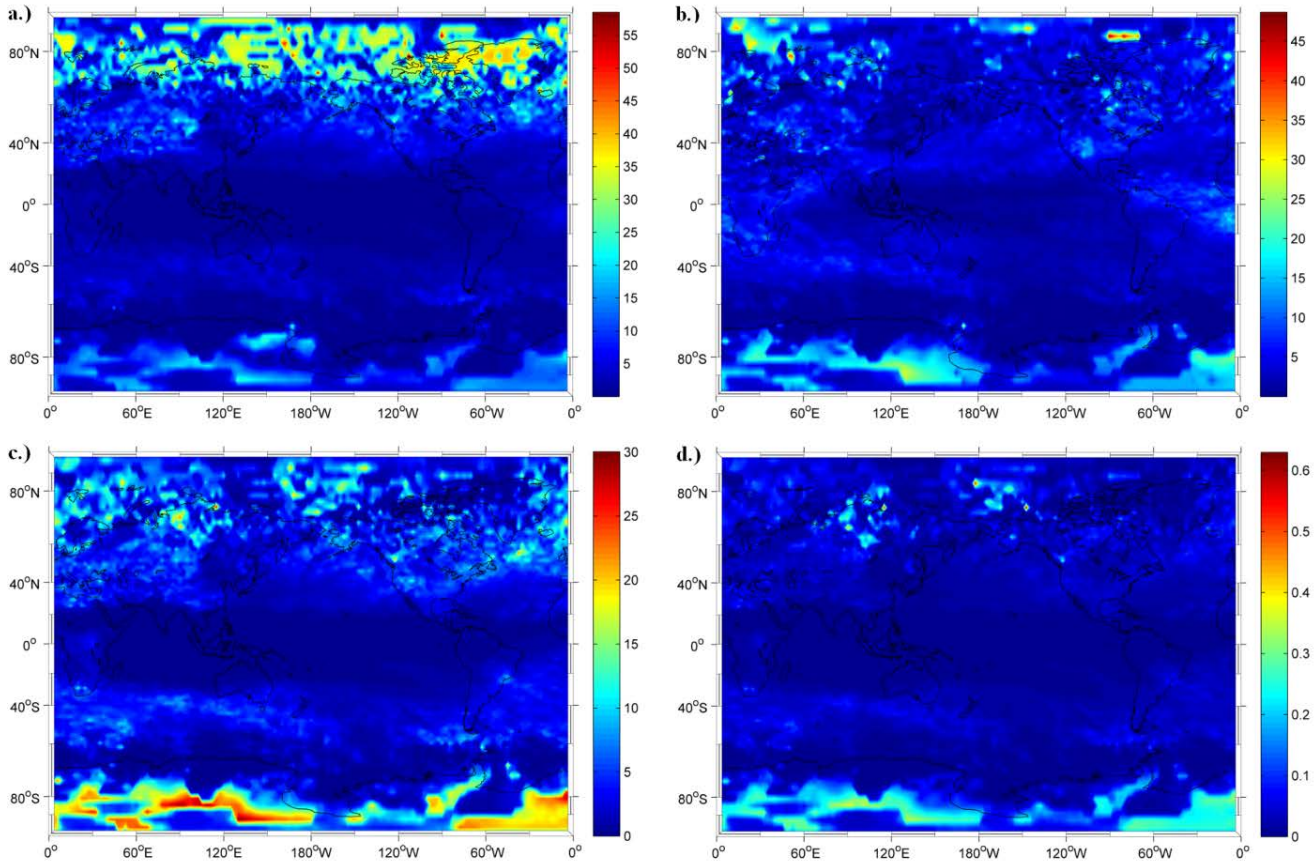

Figure 23: Annually averaged distributions of the ratio of fully normalized sensitivities to normalized standard deviations of; a.) Accumulation mode dust geometric mean diameter, b.) Coarse mode dust geometric mean diameter, c.) Black carbon geometric mean diameter, d.) Organic carbon geometric mean diameter

Global distributions of the ratio of fully normalized sensitivities to fully normalized variability are presented in Figure 21, Figure 22, and Figure 23 for all fields found in the third column of Table 3.

4.3 The Global Influence of Model Variables on Variability of Crystal Number Concentration

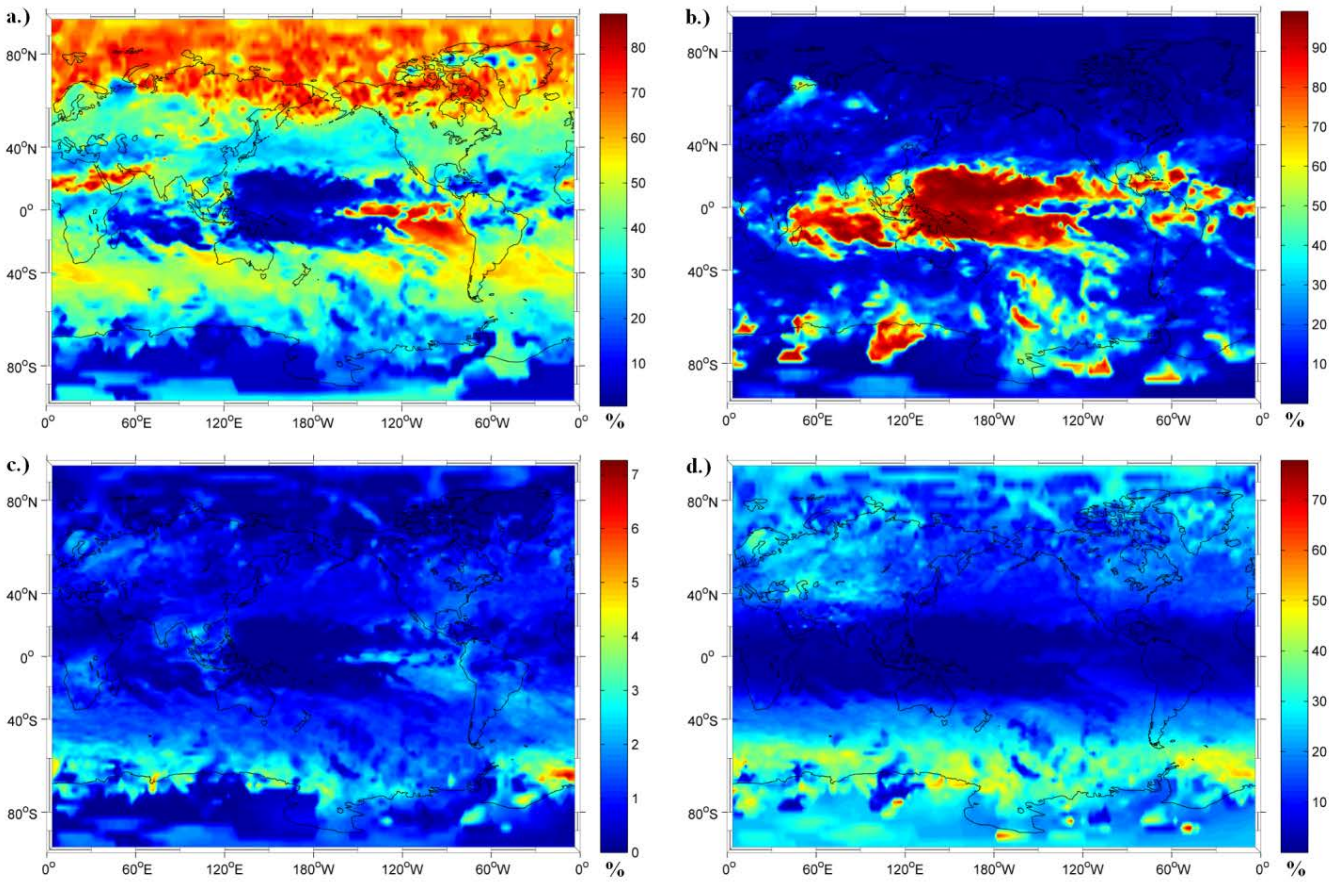

Figure 24: Annually averaged percent contributions of model variables to σN_i for; a.) Updraft velocity, b.) Sulfate number concentration, c.) Sulfate geometric mean diameter, d.) Temperature.

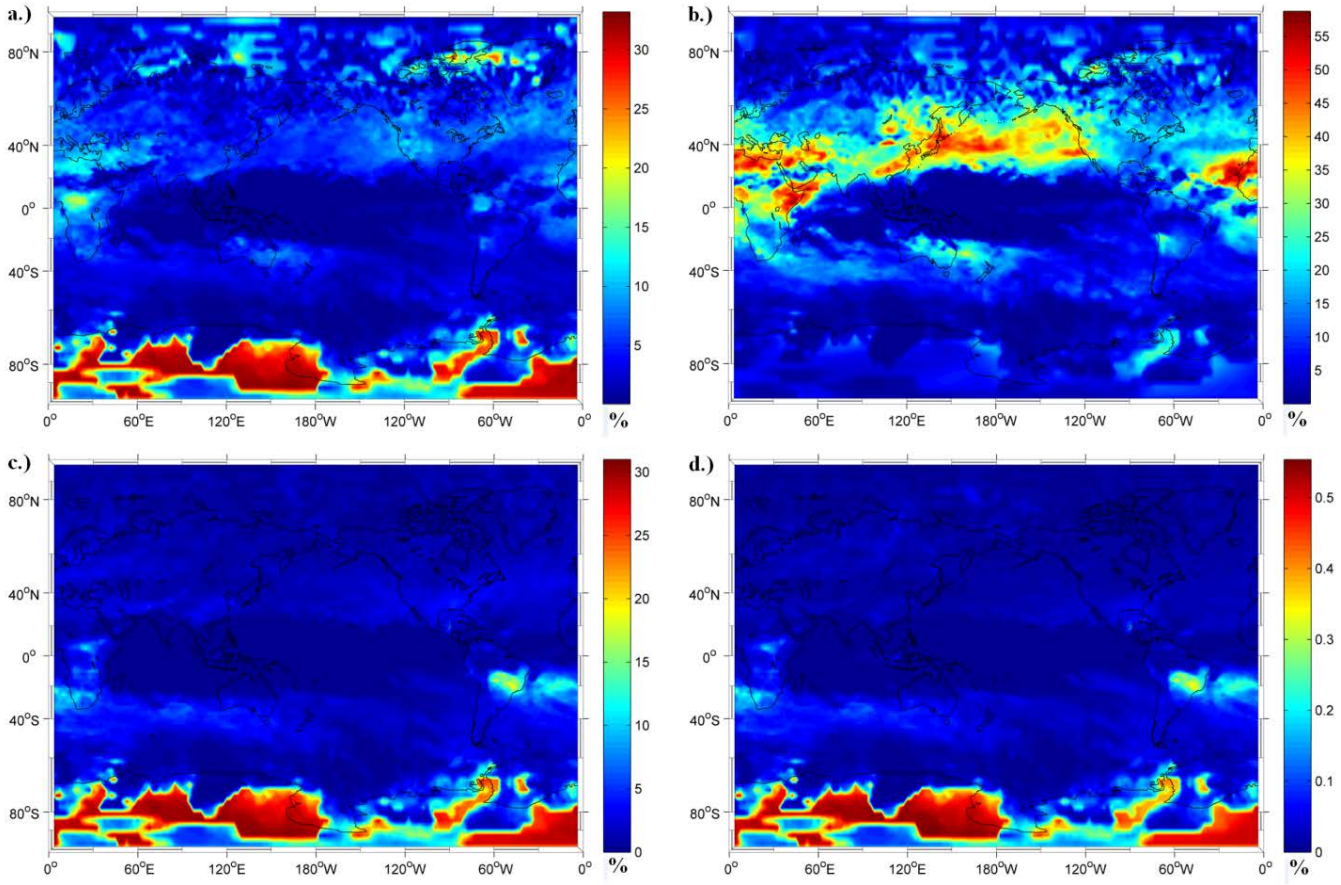

Figure 25: Annually averaged percent contributions of insoluble aerosol number concentration to σN_i for; a.) Accumulation mode dust, b.) Coarse mode dust, c.) Black carbon, d.) Organic carbon.

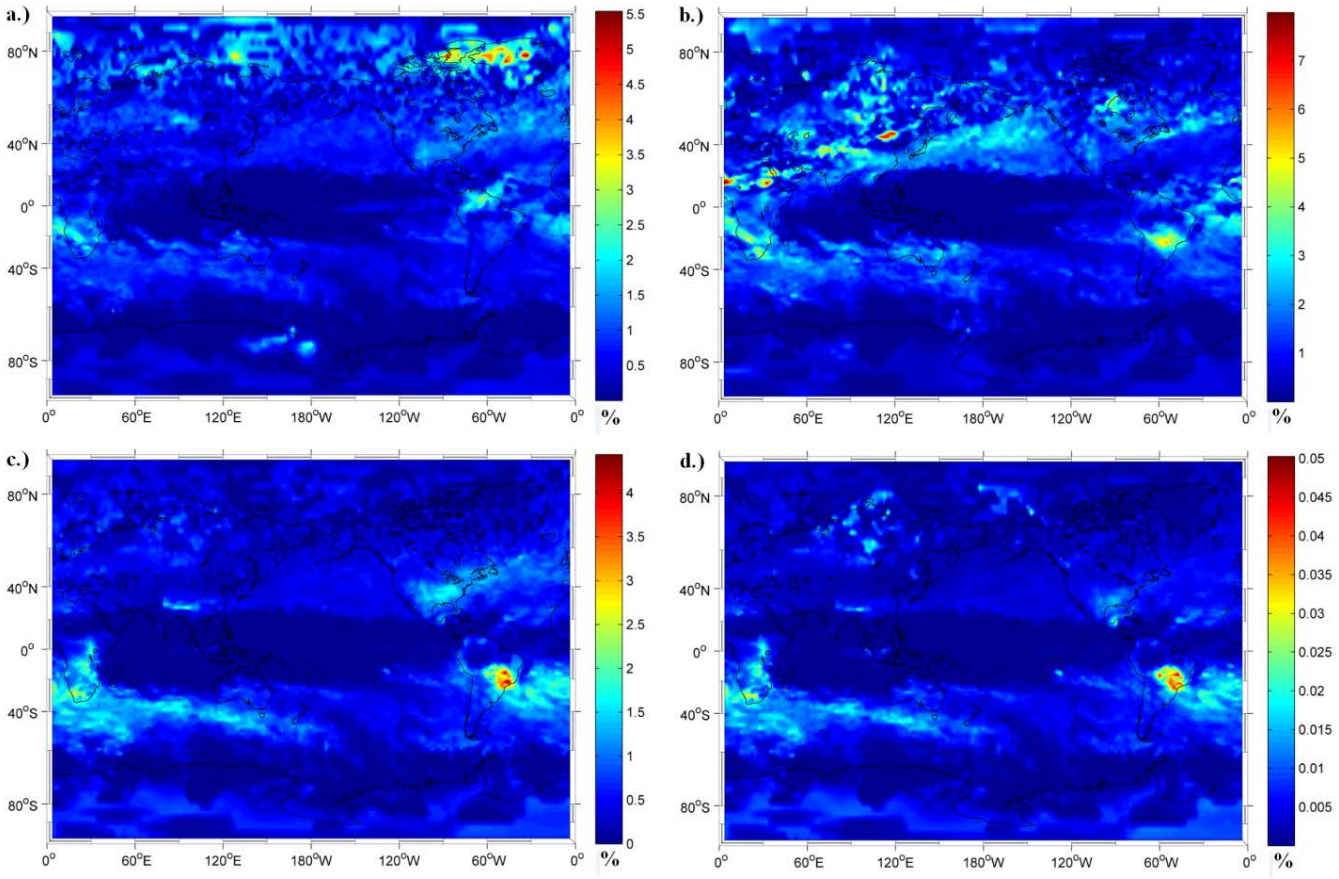

Figure 26: Annually averaged percent contributions of insoluble aerosol geometric mean diameter to σN_i for; a.) Accumulation mode dust, b.) Coarse mode dust, c.) Black carbon, d.) Organic carbon.

The global distributions of $\xi N_i x_j$ as percentages are shown in Figure 24, Figure 25, and Figure 26 and are discussed in detail in the following sections.

4.3.1 Updraft Velocity, Soluble Aerosol Characteristics, and Temperature

Figure 24 shows the global distribution of $\xi N_i x_j$ for updraft velocity, sulfate number concentration and geometric mean diameter, and temperature. Averaged globally, updraft velocity contributes to 38.20% of σN_i, with the strongest influence in the high latitudes of the Northern Hemisphere where the contribution is as high as 87%. w impacts σN_i through contributions from both $\partial N_i/\partial w$ and modeled σw as the global averaged ratio

of these two terms is roughly equal to unit ($\partial N_i/\partial w|_n / \sigma w|_n$ = 1.11). In the high latitudes of the Northern Hemisphere, $\xi N_i w$ is highest (~85%), despite the presence of high insoluble aerosol concentrations. Although insoluble aerosol number concentration variability is high in these regions, low sensitivities of N_i to insoluble aerosol number for all aerosol species drive weak contributions from insoluble aerosol to σN_i. In the high latitudes of the Southern Hemisphere, $\xi N_i w$ weakens and is a result of strong influences from other fields, especially insoluble aerosol concentrations as sensitivity of N_i to insoluble aerosol is highest here. $\xi N_i w$ is lowest (1-10%) over the tropics where homogeneous freezing dominates crystal production. Over this region, sulfate number influences are the main contributor to σN_i due to its previously mentioned sulfate limited nature. Interestingly, the regions where w controls N_i (the tropics) are very different than the regions where w influences σN_i (mid and high latitudes).

When averaged globally, N_{sulf} contributes to 23.25% of σN_i, with its importance concentrated over the tropics where contributions are as high as ~95% as seen in Figure 24b. Shown in Table 3, these large contributions are driven mostly by high $\partial N_i/\partial N_{sulf}$ values compared to variability in modeled sulfate concentrations, with an average global ratio of these two equal to 1.42. It is important to point out that this ratio is a global average and can be as high as 60 over the regions where $\xi N_i N_{sulf}$ from sulfate number concentration is highest, further pointing to the importance of how BN09 responds to changes in N_{sulf}. Again, the magnitudes of sensitivities over the tropics is a result of the previously discussed strong potential for crystal formation here where w is globally the strongest but N_{sulf} is consistently limiting. $\xi N_i N_{sulf}$ decreases at higher latitudes as w scales decrease and the sulfate limited effect weakens, especially in the Northern Hemisphere.

In the Southern Hemisphere, spotty areas of higher contributions of N_{sulf} to σN_i can be observed which spatially correlate with weak sensitivities to temperature and small contributions from other fields to σN_i, allowing the influence of N_{sulf} to be more prominent.

At a value of 0.983%, the global average $\xi N_i D_{sulf}$ is relatively insignificant which can be seen in Figure 24c. $\xi N_i D_{sulf}$ comes about through equal contributions from both $\partial N_i/\partial D_{sulf}$ and σD_{sulf} as the ratio of normalized sensitivities to variability is 1.05. Despite the relative low annually averaged percent contribution of D_{sulf} to σN_i, percent contributions can be as high as 7.2% in parts of the Southern Hemisphere where $\partial N_i/\partial D_{sulf}$ is moderate. This band of high percent contribution occurs where uniform, highly variable values of σD_{sulf} are collocated with the mentioned moderate sensitivities to D_{sulf} . This suggests that over these regions σD_{sulf} dictates the magnitude of $\xi N_i D_{sulf}$ while $\partial N_i/\partial D_{sulf}$ influences the spatial extent of the percent contribution.

As seen in Figure 24d, over the high latitudes of the Northern Hemisphere and Southern Hemisphere, the influence of temperature on σN_i is as highest with percent contributions reaching 78% and 50% respectively; when globally averaged, percentages are equal to 15.71%. $\xi N_i T$ is largest where temperatures are coldest (< 205 K) and crystal production is dominated by heterogeneous freezing. These global maxima in $\xi N_i T$ occur over regions where $\partial N_i/\partial T$ is the lowest and temperature variability is highest (~7 K); the annually averaged fully normalized ratio of temperature sensitivities to variability is 1.51×10^3, reflecting the highly sensitive nature of N_i to temperature. Despite this clear importance of sensitivities to temperature, the contribution of temperature to σN_i is low

where $\partial N_i/\partial T$ is highest (the tropics), and is a result of the important influence of other variables on σN_i here such as N_{sulf} and w.

4.3.2 Insoluble Aerosol Number Concentration

The global distributions of $\xi N_i x_j$ for dust, black carbon, and organic carbon number concentration are presented in Figure 25. $N_{dust,a}$ and $N_{dust,c}$ contribute to σN_i with a global average of 5.012% and 11.73% respectively but approach percentages as high as 33.10% and 58.20% respectively. $N_{dust,a}$ contributes to σN_i strongest in the high latitudes of the Southern Hemisphere where $\partial N_i/\partial N_{dust,a}$ are moderate and where other model fields are less important. For accumulation mode dust number, the globally averaged ratio of sensitivity to variability is equal to 0.23, suggesting variability in dust number is more important globally than inherent model sensitivities. Regardless of this, where $\xi N_i N_{dust,a}$ is largest, this ratio is as high as 2.7. This reflects that sensitivities to accumulation dust number are more important that variability where $\xi N_i N_{dust,a}$ is highest. The globally averaged ratio of sensitivity to variability for coarse mode dust number concentration is equal to 0.13, also suggesting variability in dust number is more important globally than inherent model sensitivities. Contrary to what was seen for accumulation mode dust number, the ratio of normalized sensitivities to variability for coarse mode dust over the regions where $\xi N_i N_{dust,c}$ is highest is still less than unity. This means that modeled variability in coarse mode dust number concentration drives most of $\xi N_i N_{dust,c}$ where $\xi N_i N_{dust,c}$ is the strongest. This suggests that for accumulation mode dust number, intrinsic model sensitivities (descriptions of the relevant physics) control contributions to σN_i whereas for coarse mode dust, variability in dust number does.

In the high latitudes of the Southern Hemisphere where $\partial N_i/\partial N_{bc}$ is largest in magnitude and contributions from other model fields are small, N_{bc} can account for as much as 32.3% of σN_i. Over such regions, the contribution to σN_i is driven by intrinsic model sensitivities of N_i to black carbon number concentration, as reflected by the normalized ratio of sensitivity to variability for black carbon of 2.5. Outside of these localized regions where $\xi N_i N_{bc}$ is low, normalized sensitivity to variability ratios are roughly equal to zero, making the global average value equal to 3.121%.

N_{org} influences σN_i weakly on global scales, with an average value of $\xi N_i N_{org}$ equal to 0.052% and global normalized ratios of sensitivities to variability of 2.30×10^{-3}. Over regions of highest $\xi N_i N_{org}$, this ratio approaches 0.044, revealing that organic carbon variability is the major driver σN_i from N_{org}. Regardless, in these regions $\xi N_i N_{org}$ only reaches 0.55%, elucidating the small role organic carbon plays in influencing σN_i on both regional and global scales. ξN_i from organic carbon has a very similar spatial extent to that of accumulation mode dust and black carbon number, with their importance focused over the Southern Hemisphere where other fields have little influence on σN_i. These similarities in spatial patterns are driven by similar spatial patterns of sensitivities and variability in insoluble aerosol number (since for all these species, number is computed from the same aerosol mode in CAM 5.1).

4.3.3 Insoluble Aerosol Geometric Mean Diameter

The global influence of insoluble aerosol geometric mean diameter on σN_i for all insoluble aerosol species is presented in Figure 26. $D_{dust,a}$ and $D_{dust,c}$ contribute spatially to σN_i similarly to their respective number concentrations; the largest influence occurs in

the Northern Hemisphere where heterogeneous freezing and accumulation and coarse mode dust concentrations are highest. Here $D_{dust,a}$ influences on $\xi N_i D_{dust,a}$ are as high as 5.5%, although globally $D_{dust,a}$ contributes to only 0.577%. This percent influence is primarily driven by $\partial N_i/\partial D_{dust,a}$ as the fully nomalized ratio is 5.18, suggesting dust diameter variability influences σN_i weakly, especially in the Northern Hemisphere where the magnitude of $\partial N_i/\partial D_{dust,a}$ is largest. $D_{dust,c}$ contributes up to 7.8% of σN_i over localized regions of strong dust events but only to 0.952% globally. Similarly to $D_{dust,a}$, this contribution is driven in the Northern Hemisphere by large $\partial N_i/\partial D_{dust,c}$ values, as the normalized coarse dust diameter ratio of sensitivity to variability is 4.00.

In highly localized regions over South America, the contribution of D_{bc} to σN_i approaches 4.5% with a weak average global contribution of 0.411%. Like dust, this spatial variability is driven by the relatively large magnitudes of $\partial N_i/\partial D_{bc}$ in the Northern Hemisphere and Southern Hemisphere, where the ratio of normalized sensitivities to variability is as high as 30 and equal to 3.18 when averaged globally. Despite the highly sensitive dependence of N_i on D_{bc}, low variability in D_{bc} (~ 0.03 μm) drives relatively small contributions to σN_i. Even though the daily variability in D_{bc} is small globally, regions of higher variability (0.045 μm) correspond spatially to regions of highest $\xi N_i D_{bc}$, suggesting $\xi N_i D_{bc}$ may become important if anomalously high fluctuations in D_{bc} occur.

The influence of D_{org} on σN_i has nearly the same spatial extent as that of black carbon, owing to the fact that their variability in geometric mean diameter is the same. In regions over South America and Southern Africa, the contribution of D_{org} to σN_i approaches 0.05% with a weak average global contribution of 0.004%. Different from the geometric mean diameter influences from the other insoluble species, the contribution of

D_{org} to σN_i is driven by the variability in D_{org} over sensitivity, with a global average ratio of these two terms equal to 0.03. Like N_{org}, this is due to the weak ice nucleating ability of organics in PDA 2008 resulting in an insensitive dependence of N_i to organics within BN09. This suggests any changes in variability in D_{org} will directly relate to changes $\xi N_i D_{bc}$, although because sensitivities to D_{org} are low, this effect will be small.

For all insoluble aerosol, the geometric mean diameter of each lognormal size distributions has relatively minor influences on σN_i, and is focused outside the tropics where heterogeneous freeing percentage is highest. These results suggest that despite frequent model realizations at states where crystal production is dominated by heterogeneous freezing, the geometric mean diameter of insoluble aerosol play only weak, localized roles in influencing σN_i and tend to be unimportant on global scales.

4.4 Reconstructing Variability in Crystal Number Concentration with Model Fields

Using the values of $\xi N_i x_j$ for all fields presented above, we now attempt to determine the number of fields needed to capture most of σN_i. Figure 27 presents the cumulative contribution of each $\xi N_i x_j$ to σN_i as a function of each x_j. As one moves from left to right on the horizontal axis of Figure 27, each x_j is of decreasing $\xi N_i x_j$. It can be seen that with only w, N_{sulf}, and T, nearly 80% of σN_i can be captured on global scales. Furthermore, by considering only three additional terms, $N_{dust,c}$, $N_{dust,a}$, and N_{bc}, more than 95% of σN_i is captured.

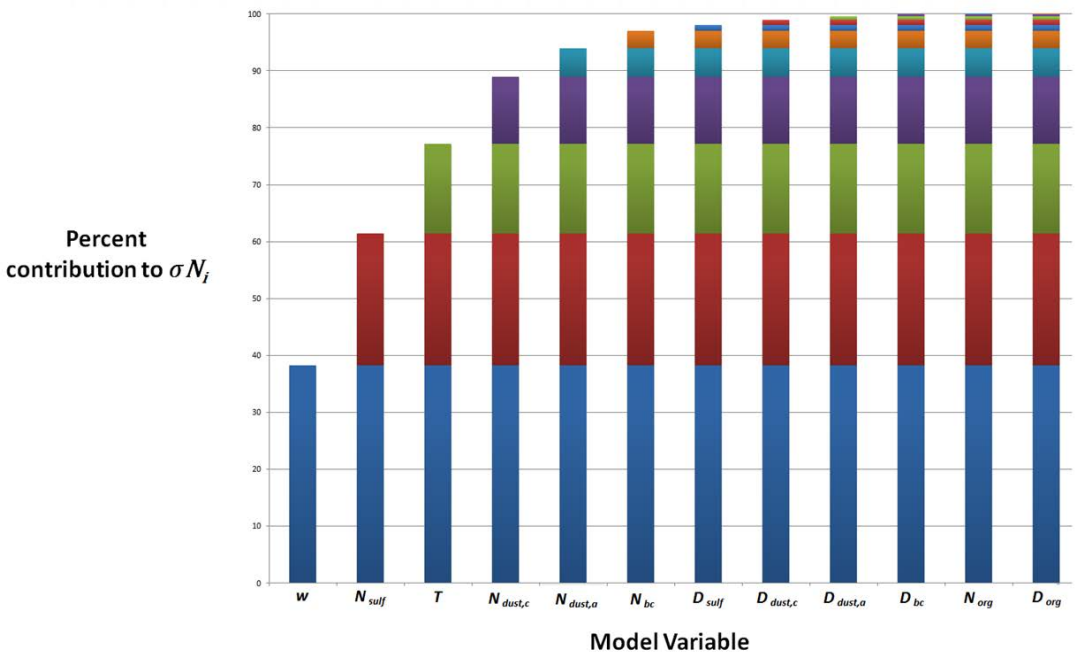

Figure 27: Cumulative globally averaged percent contributions to σN_i as a function of model variables.

This suggests that by considering the number concentration of only three of the four insoluble aerosol species, nearly all of the variability in N_i can be described. This shows that the geometric mean diameter of soluble and insoluble aerosol need not be considered when quantifying drivers of σN_i. Additionally, the role of organic carbon in influencing σN_i is minor for both number and geometric mean diameter. Although these results partially ignore the regional role that individual fields play on σN_i (only N_{sulf} field is needed to describe the variability in N_i over the tropics), they do capture annual global influences of all fields on σN_i. In future analyses, Figure 27 should be constructed for individual regions of the globe where different, unique collections of variables are needed to capture the majority of σN_i.

CHAPTER 5

CONCLUSIONS

5.1 Conclusions

The novel approach of adjoint sensitivity analysis is shown to efficiently compute the sensitivity of formed ice crystal number concentration to: updraft velocity, soluble aerosol number concentration and size, insoluble aerosol number concentration and size, and ice deposition coefficient. Sensitivities were computed with the adjoint model of the Barahona and Nenes ice parameterization family which describes ice formation upon preexisting soluble and insoluble aerosol particles within an air parcel ascending at a constant updraft velocity, temperature, and pressure. The adjoint model was developed using the automatic differentiation tool TAPENADE and was implemented in the CESM Community Atmosphere Model Version 5.1 global model where sensitivities were computed at the 232.6 hPa. The direct sensitivity information was then extended to understand the extent to which each of these model fields drive variability in formed crystal number concentration within this global model.

The global sensitivity of formed crystal number concentration to updraft velocity is positive and largest over the tropics where strong surface heating and converging winds result in strong atmospheric turbulence and cloud forming updraft velocity. Formed crystal number concentration sensitivity to sulfate number concentration is largest over the tropics where adequate supersaturation generation is available from strong updrafts but sulfate number concentration is low, suggesting a sulfate limited region. This suggests that sulfate number concentration can strongly control formed

crystal number concentration, although this effect is secondary to that of updraft velocity. Sulfate diameter and ice deposition coefficient sensitivities have a similar spatial pattern with opposite signs; increases in deposition coefficient tends to cause increased depletion of supersaturation during cloud formation resulting in lower formed crystal number concentration values; conversely, increasing the size of sulfate particles increases the fraction of the population of supercooled droplets that will freeze, increasing formed crystal number concentration. The sensitivity of formed crystal number concentration to temperature is negative in sign and largest in magnitude over regions where heterogeneous freezing percentage is low and updraft velocity is highest; over strong dust events, sensitivities to temperature change sign with relatively weak magnitudes due to increases in the water diffusivity of water vapor. Sensitivities of formed crystal number concentration to insoluble aerosol number concentration for accumulation and coarse mode dust, black carbon, and organic carbon all are negative in sign, even though heterogeneous freezing is the dominant mode of crystal production. This inconsistency is explained by the time series of updraft velocity and sensitivities of formed crystal number concentration to insoluble aerosol number concentration; here it's seen that extreme event of anomalously high updraft velocity shift the model state of the activation parameterization to regimes of combined homogeneous and heterogeneous freezing where sensitivities to insoluble number are large in magnitude and negative in sign, making the annually averaged sensitivities to insoluble aerosol number negative. All sensitivities to the geometric mean diameters of insoluble aerosol size distributions have similar spatial structures where three distinct sensitivity regimes can be observed. The first regime is over the tropics where homogeneous freezing is the dominant mode of

crystal production. In this region, sensitivities to insoluble aerosol geometric mean diameter are negative and small in magnitude due to strong updrafts buffering transitions to pure heterogeneous freezing. Over the mid-latitudes of both the Northern Hemisphere and Southern Hemisphere, weaker updrafts and moderate insoluble aerosol concentrations drive frequent transitions in freezing regimes, resulting in large, negative sensitivities. This constitutes the second freezing regime, found over high concentrations of dust and heterogeneous freezing percentages; here transitions to combined homogeneous and heterogeneous freezing are infrequent, resulting in small, positive sensitivities to insoluble aerosol geometric mean diameter.

Updraft velocity is responsible for more than 85% of the modeled variability in formed crystal number concentration in the mid and upper latitudes of both the Northern Hemisphere and as much as 60% over the mid-latitudes of the Southern hemisphere. Sulfate number concentration is responsible for nearly all modeled variability of formed crystal number concentration throughout all of the tropics due to large sensitivities of formed crystal number concentration to sulfate number and high variability in sulfate number concentration, consistent with the notion of a sulfate controlled regime of the model. Even though updraft velocity is responsible for most of the spatial structure of formed crystal number concentration in the tropics, we see from this work that sulfate number concentration controls the variability in formed crystal number concentration in this region. In the high latitudes of the Southern Hemisphere, temperature is responsible for 30 – 75% of the variability in formed crystal number concentration, and is likely to be more important at higher altitudes where temperatures are lower. The spatial role of insoluble aerosol species on variability in formed crystal number concentration is highly

localized and isolated to the Southern Hemisphere where insoluble aerosol concentrations are lowest. On global scales, updraft velocity, sulfate number concentration, and temperature are responsible for 85% of the variability in formed crystal number concentration. Including only the number concentrations of accumulation and coarse mode dust and black carbon, over 95% of the variability in formed crystal number concentration can be captured. These results may vary depending on model assumptions and the description of heterogeneous nucleation, but the soundness of the underlying physics suggests that adjoint sensitivity analysis is a tool that can provide valuable insights into the basis of model tendencies and modeled variability of microphysical properties within large scale atmospheric models.

REFERENCES

[1] Stevens, B., and Feingold, G. (2009). Untangling aerosol effects on clouds and precipitation in a buffered system. *Nature, 461*(7264), 607–13. doi:10.1038/nature08281.

[2] Stocker, T.F., D. Qin, G.-K. Plattner, L.V. Alexander, S.K. Allen, N.L. Bindoff, F.-M. Bréon, J.A. Church, U. Cubasch, S. Emori, P. Forster, P. Friedlingstein, N. Gillett, J.M. Gregory, D.L. Hartmann, E. Jansen, B. Kirtman, R. Knutti, K. Krishna Kumar, P. Lemke, J. Marotzke, V. Masson-Delmotte, G.A. Meehl, I.I. Mokhov, S. Piao, V. Ramaswamy, D.Randall, M. Rhein, M. Rojas, C. Sabine, D. Shindell, L.D. Talley, D.G. Vaughan and S.-P. Xie, 2013: *Technical Summary. In: Climate Change 2013: The Physical Science Basis. Contribution of Working Group I to the Fifth Assessment Report of the Intergovernmental Panel on Climate Change* [Stocker, T.F., D. Qin, G.-K. Plattner, M. Tignor, S.K. Allen, J. Boschung, A. Nauels, Y. Xia, V. Bex and P.M. Midgley (eds.)]. Cambridge University Press, Cambridge, United Kingdom and New York, NY, USA.

[3] Boucher, O., D. Randall, P. Artaxo, C. Bretherton, G. Feingold, P. Forster, V.-M. Kerminen, Y. Kondo, H. Liao, U. Lohmann, P. Rasch, S.K. Satheesh, S. Sherwood, B. Stevens and X.Y. Zhang, 2013: *Clouds and Aerosols. In: Climate Change 2013: The Physical Science Basis.* Contribution of Working Group I to the Fifth Assessment Report of the Intergovernmental Panel on Climate Change[Stocker, T.F., D. Qin, G.-K. Plattner, M. Tignor, S.K. Allen, J. Boschung, A. Nauels, Y. Xia, V. Bex and P.M. Midgley (eds.)]. Cambridge University Press, Cambridge, United Kingdom and New York, NY, USA.

[4] Barahona, D. and Nenes, A. (2008), Parameterization of cirrus cloud formation in large scale models: Homogeneous nucleation, *J.Geoph.Res., 113,* D11211, doi:10.1029/2007JD009355.

[5] Barahona, D. and Nenes, A. (2009), Parameterizing the competition between homogeneous and heterogeneous freezing in cirrus cloud formation - polydisperse ice nuclei, *Atmos.Chem.Phys., 9,* 5933-5948, doi:10.5194/acp-9-5933-2009.

[6] Pruppacher, H. R. and Klett, J.D. (1997), *Microphysics of Clouds and Precipitation 2nd ed.*, Kluwer Academic Publishers, Boston, MA USA.

[7] Khvorostyanov, V. I. and Curry, J. A. (2004), The theory of ice nucleation by heterogeneous freezing of deliquescent mixed CCN. Part I: critical radius, energy and nucleation rate, *J.Atmos.*Chem., *61*, 2676-2691, doi:10.1175/JAS3266.1.

[8] Jensen, E. J. et al. (1996), Dehydration of the upper troposphere and lower stratosphere by subvisible cirrus clouds near the tropical tropopause, *Geoph.Res.Let., 23,* (8), 825-828, doi:10.1029/96GL00722.

[9] Jensen, E. J., Diskin, G., Lawson, R. P., Lance, S., Bui, T. P., Hlavka, D., McGill, M., et al., (2013), Ice nucleation and dehydration in the Tropical Tropopause Layer, *Proceedings of the National Academy of Sciences of the United States of America*, *110*, (6), 2041-2046., doi:10.1073/pnas.1217104110.

[10] Dessler, A. E., Minschwaner, K., Weinstock, E. M., Hintsa, E. J., Anderson, J. G., and Russell, J. M. (1996), The effects of tropical cirrus clouds on the abundance of lower stratospheric ozone, *J.Atmos.Chem.*, *23*, (2), 209-220, doi:10.1007/BF00048261.

[11] Shindell, D. T. (2001), Climate and ozone response to increased stratospheric water vapor, *Geoph.Res.*Let., 28, 8, 1551-1554, doi:10.1029/1999GL011197.

[12] Lohmann, U. and Feichter, J. (2005), Global indirect aerosol effects: a review, *Atmos.Chem.Phys.*, *5*, 715-737, doi:10.5194/acp-5-715-2005.

[13] Barkstrom, B. R. and Smith, G.L. (1986), The Earth Radiation Budget Experiment: Science and implementation, Rev. Geophys., 24(2), 379–390, doi:10.1029/RG024i002p00379.

[14] Liou, K.N. (1986), Influence of Cirrus Clouds on Weather and Climate Processes: A Global Perspective, *Monthly Weather Review*, *114*, 1167-1199.

[15] Ramanathan, V. and Collins, W. (1991), Thermodynamic regulation of ocean warming by cirrus clouds deduced from observations of 1987 El Nino, *Nature*, *351*, 27-32, doi:10.1038/351027a0.

[16] Lynch, D.K. (1996), Cirrus clouds: their role in climate and global change?, *Acta Astonautica*, *38*, (1), 859-863.

[17] Barahona, D. and A. Nenes (2011), Dynamical states of low temperature cirrus, *Atmos.Chem. Phys*., *11*, 3757-3771, doi:10.5194/acp-11-3757-2011.

[18] Bougiatioti, A., Nenes, A., Fountoukis, C., Kalivitis, N., Pandis, S. N., & Mihalopoulos, N. (2011), Size-resolved CCN distributions and activation kinetics of aged continental and marine aerosol. *Atmos. Chem. and Phys*,, 11(16), 8791–8808. doi:10.5194/acp-11-8791-2011.

[19] Kumar, P., Sokolik, I. N., & Nenes, A. (2011), Cloud condensation nuclei activity and droplet activation kinetics of wet processed regional dust samples and minerals. *Atmos. Chem. and Phys.*, 11(16), 8661–8676. doi:10.5194/acp-11-8661-2011.

[20] Koop, T., Luo, B., Tslas, A., and Peter, T. (2000), Water activity as the determinant for homogeneous ice nucleation in aqueous solutions, *Nature*, 406, 611-614.

[21] Hoose, C. and Möhler, O. (2012), Heterogeneous ice nucleation on atmospheric aerosols: a review of results from laboratory experiments, *Atmos.Chem.Phys.*, *12*, 9817-9854, doi:10.5194/acp-12-9817-2012.

[22] Abbatt, J.P.D., Benz, S., Cziczo, DJ., Kanji, Z., Lohmann, U., Möhler, O. (2006), Solid Ammonium Sulfate Aerosols as Ice Nuclei: A Pathway for Cirrus Cloud Formation, *Science*, *313*, 1770, doi:10.1126/science1129726.

[23] Murray, B.J., Wilson, T.W., Dobbie, S., Cui, Z.Q., Al-Jumur S.M.R.K., Mohler, O., Schnaiter, M., Wagner, R., Benz, S., Niemand, M., Saathoff, H., Ebert, V., Wagner, S., Kärcher, B. (2010), Heterogeneous nucleation of ice particles on glassy aerosols under cirrus conditions, *Nature Geoscience*, *3*, 233-237, doi:10.1038/NGEO817.

[24] Barahona, D., Rodriguez, J., and Nenes, A. (2010), Sensitivity of the global distribution of cirrus ice crystal concentration to heterogeneous freezing, *J.Geoph.Res.*, *115*, (D23213), doi:10.1029/2010JD014273.

[25] DeMott, P. J., Möhler, O., Stetzer, O., Vali, G., Levin, Z., Petters, M. D., Murakami, M., et al., (2011), Resurgence in Ice Nuclei Measurement Research, *Bulletin of the American Meteorological Society*, *92*, (12), 1623-1635, doi:10.1175/2011BAMS3119.1.

[26] Kärcher, B. and Ström, J. (2003), The roles of dynamical variability and aerosols in cirrus cloud formation, *Atmos.Chem.Phys.*, *3*, (2), 1415-1451, doi:10.5194/acpd-3-1415-2003.

[27] Haag, W. (2004), The impact of aerosols and gravity waves on cirrus clouds at midlatitudes, *J.Geoph.Res.*, *109*, (D12), D12202, doi:10.1029/2004JD004579.

[28] Ming, Y., Ramaswamy, V., Donner, L., Phillips, V., Klein, S., Ginoux, P., Horowitz, L. (2007), Modeling the Interactions between Aerosols and Liquid Water Clouds with a Self-Consistent Cloud Scheme in a General Circulation Model, *J. Atmos. Sci.*, *64*, 1189-1209, doi:10.1175/JAS3874.1.

[29] Carslaw, K. et al., (2013), Large contribution of natural aerosols to uncertainty in indirect forcing, *Nature*, *503*, 67-71, doi:10.1038/nature12674.

[30] Kärcher, B. and Lohmann, U. (2002), A parameterization of cirrus cloud formation: Homogeneous freezing of supercooled aerosols, *J.Geoph.Res.*, *107*, (D2), AAC 4-1-AAC 4-10, doi:10.1029/2001JD000470.

[31] Kärcher, B. (2002), A Parameterization of cirrus cloud formation: Homogeneous freezing including effects of aerosol size, *J.Geoph.Res.*, *107*, (D23), 4698, doi:10.1029/2001JD001429.

[32] Kärcher, B. (2003), A parameterization of cirrus cloud formation: Heterogeneous freezing, *J.Geoph.Res.*, *108*, (D14), 4402, doi:10.1029/2002JD003220.

[33] Kärcher, B., Hendricks, J., and Lohmann, U. (2006), Physically based parameterization of cirrus cloud formation for use in global atmospheric models, *J.Geoph.Res.*, *111*, (D1), D01205, doi:10.1029/2005JD006219.

[34] Liu, X., and Penner, J. E. (2005), Ice nucleation parameterization for global models, *Meteorologische Zeitschrift*, 14, (4), 499–514m doi:10.1127/0941-2948/2005/0059.

[35] Barahona, D. and Nenes, A. (2009), Parameterizing the competition between homogeneous and heterogeneous freezing in cirrus cloud formation - monodisperse ice nuclei, *Atmos.Chem.Phys.*, *9*, 369-381, doi:10.5194/acp-9-369-2009.

[36] Barahona, D., Molod, A., Bacmeister, J., Nenes, A., Gettelman, A., Morrison, H., Phillips, V., and Eichmann, A. (2013), Development of two-moment cloud microphysics for liquid and ice within the NASA Goddard earth observing system model (GEOS-5), *Geosci.Mod.Dev.*, *in review*.

[37] Gettelman, A., Liu, X., Barahona, D., Lohmann, U., and Chen, C. (2012), Climate impacts of ice nucleation, *J.Geoph.Res.*, *117*, 1-14, doi:10.1029/2012JD017950.

[38] Spracklen, D. V., Pringle, K. J., Carslaw, K. S., Chipperfield, M. P., and Mann, G. W. (2005), A global off-line model of size-resolved aerosol microphysics: I. Model development and prediction of aerosol properties, *Atmos.Chem.Phys.*, *5*, 2227-2252, doi:10.5194/acp-5-2227-2005.

[39] Sotiropoulou, R.E. P., Nenes, A., Adams, P.J., and Seinfeld, J.H. (2007), Cloud condensation nuclei prediction error from application of Köhler theory: Importance for the aerosol indirect effect, *J.Geoph.Res.*, *112*, D12202, doi:10.1029/2006JD007834.

[40] Lee, L.A**.,** Carslaw, K.S., Pringle, K.J., Mann, G.W. (2012), Mapping the uncertainty in global CCN using emulation, *Atmos.Chem.Phys.*, *12*, 9739-9751, doi:10.5194/acp-12-9739-2012.

[41] Karydis, V.A., Capps, S.L., Russell, A.G. and Nenes, A. (2012), Adjoint sensitivity of global cloud droplet number to aerosol and dynamical parameters, *Atmos.Chem.Phys.*, *12*, 12081-12117, doi:10.5194/acpd-12-12081-2012.

[42] Kumar, P., Sokolik, I.N., and Nenes, A. (2009), Parameterization of cloud droplet formation for global and regional models: Including adsorption activation from insoluble CCN, *Atmos.Chem.Phys.*, *9*, 2517-2532, doi:10.5194/acp-9-2517-2009.

[43] Moore, R.H., Karydis, V.L., Capps, S.L., Lathem, T.L. and Nenes, A. (2013), Droplet number prediction uncertainties from CCN: An integrated assessment using

observations and a global model adjoint, *Atmos.Chem.Phys.*, *13*, 4235-4251, doi:10.5194/acp-13-4235-2013.

[44] Morales Betancourt, R. and Nenes, A. (2013), Aerosol activation parameterization: The population splitting concept revisited, *Geosci.Mod.Dev., in review*.

[45] Morales Betancourt, R. and Nenes, A. (2013), Understanding the contributions of aerosol properties and parameterization discrepancies to droplet number variability in a Global Climate Model, *Atmos.Chem.Phys.Dis.*, *13*, 31479-31526, doi:10.5194/acpd-13-31479-2013.

[46] Abdul-Razzak, H. and Ghan, S. (2000), A parameterization of aerosol activation: Multiple aerosol types, *J.Geoph.Res.*, *105*, (D5), 6837 - 6844, doi:10.1029/1999JD901161.

[47] Fountoukis, C. and A. Nenes, A. (2005), Continued development of a cloud droplet formation parameterization for global climate models, *J.Geoph.Res.*, *110***,** D11212, doi:10.1029/2004JD005591.

[48] Saide, P. E., Carmichael, G., Spak, S. N., Minnis, P., and Ayers, J. K. (2012), Improving aerosol distributions below clouds by assimilating satellite-retrieved cloud droplet number, *Proceedings of the National Academy of Sciences of the United States of America*, *109*, 11939-11943, doi:10.1073/pnas.1205877109.

[49] Karydis, V.A., Capps, S.L., Moore, R.H., Russell, A., Henze, D.K. and A. Nenes (2012), Using a global aerosol model adjoint to unravel the footprint of spatially-distributed emissions on cloud droplet number and cloud albedo, *Geoph.Res.Let.***,** *39***,** L24804, doi:10.1029/2012GL053346.

[50] Phillips, V., DeMott, P., and Andronache, C. (2008), An Empirical Parameterization of Heterogeneous Ice Nucleation for Multiple Chemical Species of Aerosol, *J. Atmos. Sci*., *65*, 2757-2783, doi:10.1175/2007JAS2546.1.

[51] Ren, C. and Mackenzie., A.R. (2005), Cirrus parametrization and the role of ice nuclei, *Quarterly Journal of Royal Meteorological Society*, *131*, 1585-1605, doi:10.1256/qj.04.126.

[52] Cziczo, D.J. et al. (2013), Clarifying the dominant sources and mechanisms of cirrus cloud formation, *Science*, *340*, (6138), 1320-1324, doi:10.1126/science.1234145.

[53] Hascöet, L. and Pascual, V. (2004) TAPENADE 2.1 user's guide. INRIA Technical Report #0300.

[54] Bartholomew-Biggs, M.C. (1998), Using forward accumulation for automatic differentiation of implicitly-defined functions, *Computational Optimization and Applications*, *9*, 65-84, doi:10.1023/A:101838210380.

[55] Capps, S.L., Henze, D.K., Hakami, A., Russell, A.G., and Nenes, A. (2012), ANISORROPIA: the adjoint of the aerosol thermodynamic model ISORROPIA, *Atmos.Chem.Phys.*, *12*, 527-543, doi:10.5194/acp-12-527-2012.

[56] Molod, A., Takacs, L., Suarez, M., Bacmeister, J., Song, I., and Eichmann, A. (2012), The GEOS-5 Atmospheric General Circulation Model: Mean Climate and Development from MERRA to Fortuna, *Technical Report Series on Global Modeling and Data Assimilation*, 28.

[57] Neale, R. B., Chen, C.C., Gettelman, A., Lauritzen, P. H., Park, S., Williamson, D. L., Conley, A. J., Garcia, R., Kinnison, D., Lamarque, J.-F., Marsh, D., Mills, M., Smith, A. K., Tilmes, S., Vitt, F., Cameron-Smith, P., Collins, W. D., Iacono, M. J., Easter,R. C., Ghan, S. J., Liu, X., Rasch, P. J., and Taylor, M. A. (2012), Description of the NCAR Community Atmosphere Model (CAM 5.0), NCAR Technical Note.

[58] Lamarque, J.-F., Bond, T. C., Eyring, V., Granier, C., Heil, A., Klimont, Z., Lee, D., Liousse, C., Mieville, A., Owen, B., Schultz, M. G., Shindell, D., Smith, S. J., Stehfest, E., Van Aardenne, J., Cooper, O. R., Kainuma, M., Mahowald, N., McConnell, J. R., Naik, V., Riahi, K., and van Vuuren, D. P. (2010), Historical (1850–2000) gridded anthropogenic and biomass burning emissions of reactive gases and aerosols: methodology and application, *Atmos.Chem.Phys*., *10*, 7017-7039, doi:10.5194/acp-10-7017-2010.

[59] Liu, X., Easter, R. C., Ghan, S. J., Zaveri, R., Rasch, P., Shi, X., Lamarque, J.-F., Gettelman, A., Morrison, H., Vitt, F., Conley, A., Park, S., Neale, R., Hannay, C., Ekman, A. M. L., Hess, P., Mahowald, N., Collins, W., Iacono, M. J., Bretherton, C. S., Flanner, M. G., and Mitchell, D. (2012), Toward a minimal representation of aerosols in climate models: description and evaluation in the Community Atmosphere Model CAM5, *Geosci.Mod.Dev*., *5*, 709-739, doi:10.5194/gmd-5-709-2012.

[60] Morrison, H. and Gettelman, H. (2008), A New Two-Moment Bulk Stratiform Cloud Microphysics Scheme in the Community Atmosphere Model, Version 3 (CAM3). Part I: Description and Numerical Tests, *J. Climate*, *21*, 3642–3659, doi:10.1175/2008JCLI2105.1.